J. Fluid Mech. (2004), *vol.* 508, *pp.* 201–239.
DOI: 10.1017/S0022112004009164 Printed in the United Kingdom

Instabilities and transition of a sphere falling or ascending freely in a Newtonian fluid

By M. JENNY, J. DUŠEK AND G. BOUCHET

Institut de Mécanique des Fluides et des Solides, ULP–CNRS UMR 7507, 2 rue Boussingault, 67000 Strasbourg, France
jenny@imfs.u-strasbg.fr; dusek@imfs.u-strasbg.fr; bouchet@imfs.u-strasbg.fr

(Received 22 July 2003 and in revised form 25 November 2003)

The scenario of transition to chaos for a sphere falling or ascending under the action of gravity in a Newtonian fluid is investigated by numerical simulation. The mathematical formulation is parameterized using two non-dimensional parameters: the solid/fluid density ratio and the generalized Galileo number expressing the ratio between the gravity–buoyancy and viscosity effects. The study is carried out fully in this two-parameter space. The results show that for all density ratios the vertical fall or ascension becomes unstable via a regular axisymmetry breaking bifurcation. This bifurcation sets in slightly earlier for light spheres than for dense ones. A steady oblique fall or ascension follows before losing stability and giving way to an oscillating oblique movement. The secondary Hopf bifurcation is shown not to correspond to that of a fixed sphere wake for density ratios lower than 2.5, for which the oscillations have a significantly lower frequency. Trajectories of falling spheres become chaotic directly from the oblique oscillating regime. Ascending spheres present a specific behaviour before reaching a chaotic regime. The periodically oscillating oblique regime undergoes a subharmonic transition yielding a low-frequency oscillating ascension which is vertical in the mean (zigzagging regime). In all these stages of transition, the trajectories are planar with a plane selected randomly during the axisymmetry breaking. The chaotic regime appears to result from an interplay of a regular and of an additional Hopf bifurcation and the onset of the chaotic regime is accompanied by the loss of the remaining planar symmetry. The asymptotic chaotic states present an intermittent character, the relaminarization phases letting the subcritical plane and periodic trajectories reappear.

1. Introduction

The motion of particles under the simultaneous action of external and hydrodynamic forces is one of the most important issues in two-phase flow from the viewpoint of both fundamental theory and applications. The classical theory based on knowledge of the creeping and laminar flow past a solid sphere, a bubble or a liquid drop yielded a variety of semi-empirical models (see e.g. Magnaudet 1997, for an exhaustive review) allowing the free-particle behaviour to be reproduced at low numerical costs and with a high degree of reliability up to a particulate Reynolds number of about 200. Beyond this limit, all 'laminar' models fail. It has been recognized that this is linked to the onset of instabilities in the system of the moving particle and surrounding fluid.

Recently, significant progress has been achieved in understanding the transition in the wake of a fixed sphere. It is widely accepted that the sphere wake loses its axisymmetry at a Reynolds number (Re) of 212 via a regular bifurcation (see Natarajan & Acrivos 1993). A steady regime characterized by a planar symmetry exists in the interval of $Re \in [212, 275]$ (Johnson & Patel 1999; Mittal 1999*a*; Ormières & Provansal 1999; Tomboulides & Orszag 2000). It has been shown in Ghidersa & Dušek (2000) that the symmetry plane is selected randomly by initial perturbations and is conserved at the secondary bifurcation, which is of Hopf type, sets in at $Re = 275$ and leads to an unsteady periodic regime. Both experiments (Ormières 1999) and numerical simulations (Mittal 1999*a*; Tomboulides & Orszag 2000) agree that the periodicity is lost beyond $Re = 300$. The loss of periodicity is linked to the loss of planarity (Mittal 1999*a*; Tomboulides & Orszag 2000) and to the onset of chaos reported by Tomboulides & Orszag (2000) at $Re = 500$.

The transition scenario of spherical particles moving freely under the action of gravity, buoyancy and hydrodynamic forces is much less clearly established. For practical experimental reasons, the earliest work was motivated by the investigation of the behaviour of the wake of a sphere moving with a constant velocity. Magarvey & Bishop (1961), Magarvey & MacLatchy (1965) and Goldburg & Florsheim (1966) are commonly cited as pioneering in the study of the fixed sphere wake. Indeed, in the laminar (axisymmetric) regime the asymptotic state is steady and the wakes of a free and of a fixed particle are identical. This is, however, not the case as soon as the loss of axisymmetry sets in. We have shown (Jenny, Bouchet & Dušek 2003) that the breaking of axisymmetry is influenced by the additional degrees of freedom of the free particle and depends on two parameters which characterize the parameter space. The first one is the density ratio ρ_0/ρ where ρ_0 is the density of the sphere (assumed to be homogeneous) and ρ is that of the fluid. The second one is the non-dimensional number characterizing the ratio of buoyant and viscous effects, to which we extended the name of Galileo number (G) commonly used for bubbly flows (e.g. Mougin & Magnaudet 2002*b*). In this paper, the number G is defined as

$$G = \frac{\sqrt{|\rho_0/\rho - 1|\, g d^3}}{\nu}, \tag{1.1}$$

where g is the acceleration due to gravity, d the sphere diameter and ν the kinematic viscosity of the fluid. It is equal to the square root of the Archimedes number (Karamanev 1996). In the following bibliographical overview we convert available data to these characteristic parameters. This provides a reference for the present work and allows the available results to be compared on a common basis. The asymptotic Reynolds number, though often used in the description of experiments, is not an external parameter, unlike for a fixed sphere placed in a uniform flow. It results rather from the equilibrium of external and hydrodynamic forces and does not have a constant value if the asymptotic regime is unsteady. In axisymmetric (laminar) regimes, numerical simulations and very well established empirical laws provide the drag coefficient C_D as a widely accepted function of the Reynolds number. The relation

$$C_D(Re_\infty) = \frac{4G^2}{3Re_\infty^2} \tag{1.2}$$

then yields an easy conversion between the asymptotic Reynolds number Re_∞ and the Galileo number G. At $Re_\infty = 212$, for example, the drag coefficient is equal to 0.753, i.e. $G = 159.3$. In the transition domain, in cases when the bibliographical references

do not provide enough data, we infer the values of G from indicated Re_∞ values by comparing them to the numerical mean Reynolds number values of simulations presented in this paper.

The early observations of Magarvey & Bishop (1961) and Magarvey & MacLatchy (1965) were those of freely falling liquid drops. On the one hand, falling drops and ascending bubbles are physically different systems, but on the other hand it is known that surface-active impurities (see e.g. Duineveld 1995) may make a small fluid inclusion behave much like a rigid sphere. Indeed, the experiments of Magarvey & Bishop (1961) and Magarvey & MacLatchy (1965) show vortex shedding very similar to that observed in the wake of a solid fixed sphere. The experiment of Magarvey & Bishop (1961) at $Re_\infty = 350$ corresponds to ρ_0/ρ between 1 and 1.6 and $G \approx 250$. The observed Strouhal number of 0.12 is very close to that of the fixed sphere wake. Similar experiments but with real solid spheres (among others at $\rho_0/\rho = 1.12$, $G = 220$) were described in Goldburg & Florsheim (1966). Their figure 6 allowed them to conclude that, at $Re = 300$, i.e. at $G \approx 220$, the wake had a significantly lower frequency: $St \approx 0.07$.

The next motivation having focused attention on the behaviour of free falling or ascending spherical particles was the issue of fluidized beds in chemical engineering in the late 1980s and early 1990s. In an experimental work, Fortes, Joseph & Lundgren (1987) were concerned mainly by the particle interaction in a system of many spherical particles maintained in suspension in an ascending stream of fluid. It is important to note that the particle regimes are not only 'definitely non-Stokesian', but even far beyond the transition threshold (particle Reynolds numbers exceeding 700). The impact of transition in the fluidization process was recognized in Karamanev & Nikolov (1992); Karamanev, Chavarie & Mayer (1996) and Karamanev (1996, 2001). The work of Karamanev *et al.* is motivated by the design of inverse fluidized beds involving particles significantly lighter than the transporting fluid. In their experiments with individual ascending particles, the authors note that the laminar models fail beyond the transition threshold, observed at a rather low particulate Reynolds number ($Re = 130$) for particles of small density ratios, $\rho_0/\rho \leqslant 0.3$. They observe a practically constant drag coefficient $C_D = 0.95$ in a wide interval of asymptotic transition regimes. The light-particle drag coefficient is thus found to be practically twice as high as that of particles characterized by density ratios $\rho_0/\rho > 0.9$, departing significantly less from classical drag laws. The particle trajectories are observed to be 'spiral' and the Strouhal numbers are comparable to those of the fixed sphere wake (between 0.1 and 0.2) in Karamanev *et al.* (1996).

Lunde & Perkins (1997) set up experiments both with bubbles and light solid spheres. The latter are made of expanded polystyrene $\rho_0/\rho = 0.05$ and their asymptotic regimes correspond to $G = 220$–350. No quantitative data are provided for their trajectories, but the verbal description states a 'chaotic motion' and an 'intermittent' wake. An acoustic velocity measurement technique brought interesting results in Mordant & Pinton (2000). Three cases correspond to the transitional regimes investigated in the present work: $\rho_0/\rho = 2.56$, $G = 227$; $\rho_0/\rho = 7.71$, $G = 183$; and $\rho_0/\rho = 7.85$, $G = 260$. The last two density ratios, those of steel spheres, are too high to yield observable oscillations of the velocity, but in the case of glass spheres ($\rho_0/\rho = 2.56$, $G = 227$), the acceleration ramps present visible oscillations. The period of oscillations is 0.125 s, i.e. taking into account the data of the paper, this corresponds to a Strouhal number of 0.055.

Much recent experimental and numerical work tackles the problem of a single bubble ascending in a quiescent fluid. Although, as already stated, this system

is different, especially if the bubbles rise in purified water, certain experiments provide data relevant for very light solid spheres. Lunde & Perkins (1997) state that a spheroidal shape of bubbles and zigzagging plane trajectories change to a spiralling motion. Ellingsen & Risso (2001) observe individual ascending bubbles ($\rho_0/\rho = 0$) at $G = 390$. From case to case, the trajectories are either zigzagging or spiral. Their data yield a Strouhal number of 0.05 and a drag coefficient of 0.2. (Note that the light-sphere data of Karamanev (2001) include the bubbles, i.e. this drag coefficient is to be compared to Karamanev's 0.95.) The numerical simulations of non-deforming ellipsoidal bubbles with various aspect ratios (Mougin & Magnaudet 2002*b*) shed light on the role of the bubble deformation in the onset of instabilities and in the trajectory behaviour. They show that, in ideally pure liquid, spherical bubbles keep a stable axisymmetric wake whatever the Galileo number G. Aspect ratios χ (ratios of the large and small half-axes of the rotation ellipsoid) exceeding 2.2 are necessary to trigger instabilities. At $\chi = 2.5$, Mougin & Magnaudet (2002*b*) reproduce the transition from a zigzagging to a helical trajectory observed, experimentally, by Lunde & Perkins (1997). Wu & Gharib (2002) paid special attention to the purity of the water in their experiments and, in spite of that, observe two different bubble forms created by different injection conditions: spherical and ellipsoidal ones. The ellipsoidal bubbles behave in agreement with expectations (spiral trajectories), whereas the spherical ones present instabilities too and their trajectories are observed to be plane and zigzagging. The authors propose a plausible explanation: shedding of residual impurities from the interface by strong initial perturbations in the process of the creation of ellipsoidal bubbles. The data concerning the spherical bubbles can thus also be considered relevant for solid spheres with a density ratio of $\rho_0/\rho = 0$. With increasing Galileo numbers G, Wu & Gharib (2002) report a vertical straight trajectory at $G = 115$, an oblique straight trajectory at $G = 159$ and trajectories zigzagging vertically in the average in a vertical plane at $G = 185, 227$ and 255. The Strouhal number of the zigzagging motion is found to be 0.087 and the drag coefficient is $C_D = 0.8$ at $Re_\infty = 300$ (i.e. $G = 230$, see (1.2)).

In conclusion, the literature allows us to expect that, in the early stages of transition, the trajectories of solid spheres are plane. At the first stage, the loss of axisymmetry yields oblique and steady trajectories. The latter lose the stability via a Hopf bifurcation and oscillations set in. The oscillations are reported to have a significantly lower Strouhal number in most investigations dealing with spheres with a density ratio lower than 3. Many uncertainties, however, remain and the picture of the scenario of transition is far from complete.

Numerical simulations are, nowadays, a very practical and reliable way of investigating transition scenarios. Apart from the numerical simulations of Mougin & Magnaudet (2002*b*), numerical work concerning free particles in transitional regimes is still practically non-existent. The simulations past a deformable liquid drop of Bozzi *et al.* (1997) are limited to axisymmetric regimes and the numerical techniques proposed by Glowinski *et al.* (2001) and Hu, Patankar & Zhu (2001) aiming at direct numerical simulations of many particle systems have been used, so far, for particulate Reynolds numbers of $Re_\infty \leqslant 118$ (Glowinski *et al.* 2001) and are restricted to sedimenting particles. On the other hand, these methods are much more powerful because they potentially allow us to tackle the still unsolved numerical problem of a deformable fluid inclusion and the many particle interactions in a sedimentation process. The ability to treat more complex systems is paid for by greater numerical costs and other limitations. For instance, the particle equations are discretized using

an explicite scheme in Glowinski *et al.* (2001), which excludes light particles (Jenny *et al.* 2003).

The investigation of the transition requires long runs and thus reduced costs of simulation. A specially adapted numerical technique is required for simulating particles of densities close to zero. A suitable technique has been proposed in Jenny *et al.* (2003) and Jenny & Dušek (2004). It meets the requirements of direct numerical simulations of the transition of light and infinitely light particles at costs not far above those of simulating a fixed sphere wake in Ghidersa & Dušek (2000). Special care is also given to numerical accuracy. The objective is achieved by solving the particle motion equation fully implicitly and exactly at each time step. The presence of the additional degrees of freedom of the moving body does not lead to any stability or accuracy reduction. The preliminary results of Jenny *et al.* (2003) show the influence of the sphere degrees of freedom on the threshold of axisymmetry breaking and confirm that for all particle densities the first stage of transition is characterized by steady oblique trajectories. The numerical results are shown to agree quantitatively with experimental observations.

The purpose of the present paper is to paint a complete picture of the transition in the two-dimensional parameter space of density ratios and Galileo numbers G. In § 2, we formulate the mathematical definition of the problem. Some additional experimental data obtained in our laboratory completing those presented above are discussed in § 3 to help in validating the simulations. Five different regimes are found during the transition. They are illustrated for light spheres of density ratio $\rho_0/\rho < 1$ in §§ 5–8. A synthetic study in the parameter space is presented in § 9. The main part of the paper is focused on the analysis of attractors. A section is added to facilitate the comparison with experiments. To what extent imperfections in the sphere fabrication might change the reported numerical results is addressed in § 10. The final discussion is presented in § 11.

2. Mathematical formulation

Unlike the wake of a fixed sphere, the problem of a freely moving solid object contains six more degrees of freedom in addition to that of the flow field. These new degrees of freedom can be described by the velocity of the centre of mass of the sphere, denoted $\boldsymbol{u}$ and the angular velocity of rotation around the centre of mass, denoted $\boldsymbol{\Omega}$. Both velocities are taken with respect to a fixed frame. The resulting physical system is made of two coupled phases. First, the fluid, the flow field of which is described by the fluid velocity $\boldsymbol{v}$ and the pressure p is perturbed by the motion of the particle. Secondly, the solid sphere is set in motion by buoyancy and gravity forces and the action of the fluid perturbs its trajectory. The fluid is characterized by its density ρ and the kinematic viscosity ν and the sphere by its density ρ_0 and its diameter d. Unlike for a fixed sphere wake, the sphere velocity is not an external parameter of the system. Instead, the effective acceleration $|\rho_0/\rho - 1|g$, where g denotes the acceleration due to gravity, can be taken as characteristic of the gravity–buoyancy effects and, as a consequence, the velocity and time units are chosen as:

$$U^* = \sqrt{|\rho_0/\rho - 1|\, gd}, \tag{2.1a}$$

$$T^* = \sqrt{\frac{d}{|\rho_0/\rho - 1|\, g}}. \tag{2.1b}$$

The flow velocity is expressed with respect to a fixed frame, but the flow field is described as a vector function of coordinates taken in a frame, the origin of which coincides with the sphere centre and which moves translationally with the sphere. The flow field then satisfies the Navier–Stokes equations non-dimensionalized with respect to the velocity scale mentioned above and the sphere diameter:

$$\frac{\partial \boldsymbol{v}}{\partial t} + [(\boldsymbol{v} - \boldsymbol{u})\cdot\nabla]\boldsymbol{v} = -\nabla\cdot p + \frac{1}{G}\nabla^2\cdot\boldsymbol{v}, \tag{2.2a}$$

$$\nabla\cdot\boldsymbol{v} = 0. \tag{2.2b}$$

Equations (2.2*a*) and (2.2*b*) involve just one parameter: the number G (1.1). They have to be completed by the boundary condition on the sphere surface S. The non-slip condition

$$\boldsymbol{v}|_S = \boldsymbol{u} + \boldsymbol{\Omega}\times\boldsymbol{r}|_S \tag{2.3}$$

is used, where $\boldsymbol{r}_S$ stands for the position vector on the sphere surface.

The velocities $\boldsymbol{u}$ and $\boldsymbol{\Omega}$ satisfy the motion equations (Jenny *et al.* 2003; Jenny & Dušek 2004)

$$\frac{\rho_0}{\rho}\frac{\mathrm{d}\boldsymbol{u}}{\mathrm{d}t} = \frac{6}{\pi}\boldsymbol{F}_{fl}(\boldsymbol{v}, p) + \boldsymbol{k}_{fix}, \tag{2.4a}$$

$$\frac{\rho_0}{\rho}\frac{\mathrm{d}\boldsymbol{\Omega}}{\mathrm{d}t} = \frac{60}{\pi}\boldsymbol{M}_{fl}(\boldsymbol{v}, p), \tag{2.4b}$$

where $\boldsymbol{F}_{fl}$ and $\boldsymbol{M}_{fl}$ are, respectively, the hydrodynamic force and torque:

$$\boldsymbol{F}_{fl}(\boldsymbol{v}, p) = \int_S \boldsymbol{f}\,\mathrm{d}S, \tag{2.5a}$$

$$\boldsymbol{M}_{fl}(\boldsymbol{v}, p) = \int_S \boldsymbol{r}_S\times\boldsymbol{f}\,\mathrm{d}S, \tag{2.5b}$$

and $\boldsymbol{k}_{fix} = \mathrm{sgn}(\rho_0/\rho - 1)\boldsymbol{g}/\|\boldsymbol{g}\|$. The elementary force $\boldsymbol{f}$ is given componentwise as:

$$f_i = \frac{2}{G}S_{ij}n_j - p\,n_i, \tag{2.6}$$

$$S_{ij} = \left(\frac{\partial v_i}{\partial x_j} + \frac{\partial v_j}{\partial x_i}\right). \tag{2.7}$$

In (2.4*a*) and (2.4*b*), the reduced density ρ_0/ρ appears as a second non-dimensional parameter of the problem.

The main numerical difficulty of the coupling between (2.2*a*)–(2.2*b*) and (2.4*a*)–(2.4*b*) consists in the necessity of using an implicit time discretization (see Jenny & Dušek 2004). This can be readily seen when the left-hand sides of (2.4*a*) and (2.4*b*) vanish for infinitely light spheres $\rho_0 = 0$. A more accurate argument presented in § 4 shows that, in fact, the numerical difficulties originate from the added mass term of the hydrodynamic force.

3. Some experimental observations

3.1. *Experimental set-up*

In parallel with the numerical investigations, we have built an experimental set-up allowing us to study the free motion of a solid sphere submitted to the action of gravity and buoyancy. The experimental configuration is made up of a Plexiglas tank allowing

a horizontal confinement smaller than 1 : 100, and a vertical confinement smaller than 1 : 1000. The asymptotic velocity of the solid sphere is controlled continuously by varying the temperature (with an accuracy of 0.1°, and a temperature difference not exceeding 0.2° between the top and the bottom of the tank) and thus the viscosity of the fluid. (Taking into account the volume of the tank, we chose water). It is also possible to control, in a discrete way, the asymptotic velocity of the sphere while varying its diameter and its density. After the sphere is released, it is followed by two cameras placed on perpendicular racks moving at the same velocity as the sphere. To measure the trajectory of the sphere in free fall or free rise, the cameras are connected directly to a computer. Image processing then determines the position of the centre of the sphere on each image: we thus obtain the coordinates on a horizontal plane. The image processing takes account of the variation of the refraction indices between the cameras and the sphere (air, Plexiglas, water) and of the crossing of the wall of the tank (plate with parallel faces). The vertical coordinate is provided by a sensor which determines the position of the cameras at every moment. The experimental device thus makes it possible to obtain the three-dimensional position of the centre of the sphere every 1/25 s, with a precision of about 0.1 diameter. For supercritical Galileo numbers G, the amplitude of the deviation from the vertical direction increases with decreasing density of particles. For the purpose of this preliminary experimental investigation, we chose ascending spheres. They are made of polypropylene, of density ranging from 0.7 to 0.9, and have diameters between 1 and 4 mm. The sphericity of the spheres is guaranteed (they are made for ball bearings). It was, however, necessary to find a reliable method of determining accurately the diameter and the density of each sphere in order to fix the Galileo number correctly. We combine, for this purpose, direct measurement of the diameter (accuracy of 0.01 mm) and weighing of mass (accuracy of 1 mg) with measuring of the free ascending velocity in the laminar (axisymmetric) regime. The reliability of the laminar drag values obtained by the same code as that used for the numerical simulations presented in the following sections allows us to guarantee a better than 2% accuracy of $\rho_0/\rho - 1$, i.e. of G.

3.2. *Preliminary experimental observations*

The first experimental observations at supercritical Galileo numbers ranging from $G = 165$ to 255 allow three phases of the instability development of the trajectory to be distinguished. The first phase corresponds to the initial acceleration until the sphere reaches the critical Reynolds number of symmetry breaking and until the wake develops sufficiently to let the symmetry breaking instability appear. In figures 1 and 2, we represent some sample trajectories at $G = 180$ for a density ratio $\rho_0/\rho = 0.89$ (the same sphere at the same water temperature). Some information on a regime at $G = 170$ for the same density ratio was published in Jenny *et al.* (2003). The Galileo number of 180 being quite significantly supercritical, the primary instability develops rather rapidly within a distance of a few diameters. The stage dominated by the primary instability corresponds to an almost straight oblique ascension modulated by the simultaneous onset of the secondary, oscillating, instability. Both the vertical and the oblique ascension are clearly visible in (*b*) figure 1, where the trajectories are restricted to a vertical distance of about 100 diameters above the injection point. The figure represents the time *vs.* the deviation from the vertical axis. This way of plotting projects all the trajectories onto the same plane. Note the random selection of the trajectory plane in figure 1(*a*).

Our water tank allows the trajectory to be followed over a distance of almost one thousand diameters. Moreover, if we follow the sphere all along the tank height, we

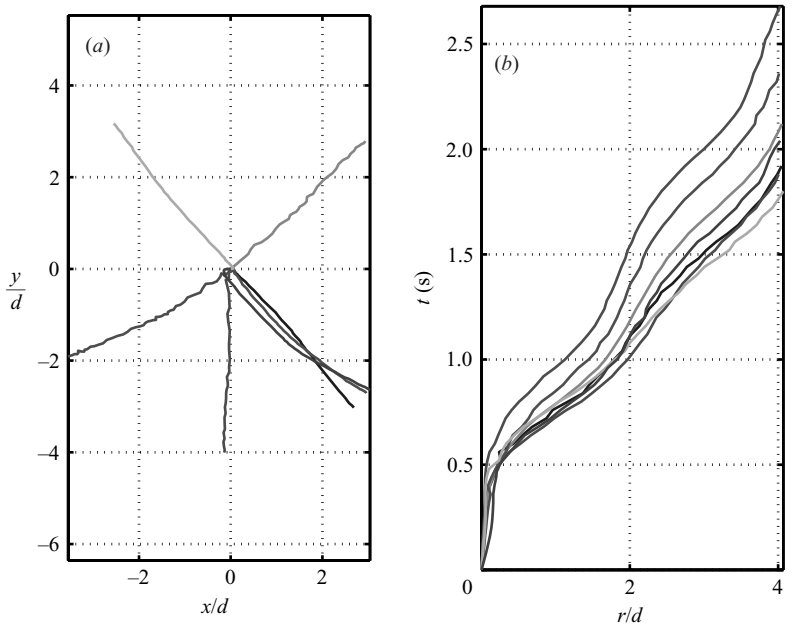

FIGURE 1. Sample trajectories projected on (*a*) a horizontal and (*b*) a vertical plane: initial phase of instability development for $Z < 100$ diameters ($\rho_0/\rho = 0.89$, $G = 180$).

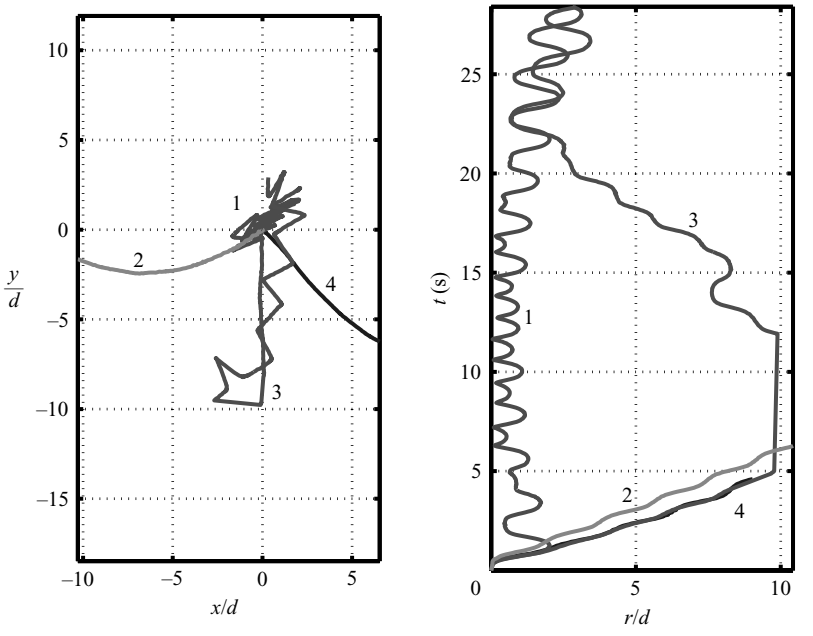

FIGURE 2. Sample trajectories projected on (*a*) a horizontal and (*b*) a vertical plane: full trajectories observed all the way up the water tank (≈ 1000 particle diameters) ($\rho_0/\rho = 0.89$ $G = 180$).

observe that the sphere sometimes ends up oscillating along a practically vertical mean direction. The transient phase between the oblique and oscillating trajectory varies considerably from one experiment to another and, at this regime, most trajectories

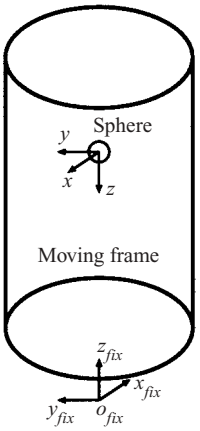

FIGURE 3. Geometry of the problem. Orientation of axes for light spheres, $\rho_0/\rho < 1$.

even escape outside the field of our image (20 diameters wide). This can be explained by a variable initial perturbation helping in the instability development. Indeed, in spite of all efforts aiming at releasing the spheres without much perturbation, the latter remains significant for the instability development and, of course, varies from one experiment to another. In figure 2(*b*), two trajectories remain close to the tank axis: numbers 1 and 3 (trajectory number 3 leaves the optic field for some time but eventually comes back). We state that the final stages of both trajectories are similar. Another striking feature is the loss of planarity of the trajectory (see figure 2(*a*)). Both trajectories observed at the full height of the tank present a random-like projection onto a horizontal plane. The experimental results presented seem to correspond to chaotic regimes analysed numerically in § 8. For the given density ratio 0.89, the onset of chaos (for perfectly homogeneous spheres) appears to be situated higher (at $G \approx 215$, see figure 29) but the behaviour is qualitatively similar. In § 10, we explain this discrepancy by the presence of an air bubble in the ball. The bubble makes the ball inhomogeneous and creates a slight eccentricity of the mass distribution. In § 10, we show that this shifts the instability thresholds lower. A more exhaustive and accurate experimental study is currently in progress with an improved temperature control system, allowing all the stages of the transition to be followed more systematically and the control parameters to be set more reliably.

4. Numerical method and validation

The numerical method has been presented in detail in Jenny & Dušek (2004). The purpose of this brief summary is to facilitate the reading of the next section.

The Navier–Stokes solver is based on a spectral–spectral-element spatial discretization in a cylindrical domain (see figure 3). The decomposition of the flow field into a series of Fourier azimuthal modes

$$p(z, r, \theta, t) = \sum_{m=-\infty}^{+\infty} p_m(z, r, t)\, \mathrm{e}^{-\mathrm{i}m\theta}, \tag{4.1a}$$

$$\boldsymbol{v}(z, r, \theta, t) = \sum_{m=-\infty}^{+\infty} \boldsymbol{v}_m(z, r, t)\, \mathrm{e}^{-\mathrm{i}m\theta}, \tag{4.1b}$$

is crucial for both theoretical and practical reasons. It allows a linear analysis of the axisymmetry breaking at the primary instability (see also Ghidersa & Dušek 2000) and reduces the computing costs significantly because the series converges extremely rapidly in the domain of transition. Only 9 Fourier components (zero to eight) need be taken into account to reach a better than 1% accuracy in a typical simulation (see Jenny & Dušek 2004).

The cylindrical domain has a radius of 8 diameters and an overall length of 37 diameters. The sphere is placed 12 diameters downstream of the inflow boundary. Figure 3 represents the orientation of the axes of the fixed and moving frame in the case of an ascending sphere ($\rho_0/\rho < 1$). If $\rho_0/\rho > 1$, the sphere falls and the moving frame is oriented in the same way as the fixed one. Both ways, the z-axis of the moving frame points in the opposite direction to the sphere's movement. The flow velocities being expressed in the fixed frame are zero far from the sphere, positive for ascending spheres and negative for falling spheres. To simulate an infinite domain, zero velocity is taken as a boundary condition on the inflow basis of the cylinder (upper basis of figure 3) and a stress-free boundary condition is imposed elsewhere in a weak sense. The latter allows vortical structures to leave the domain freely and makes the solution practically insensitive to the presence of unphysical boundaries (see Ghidersa & Dušek (2000); Jenny & Dušek (2004) for tests).

The time discretization is based on the time-splitting scheme for the Navier–Stokes equations ((2.2a) and (2.2b)) presented in Ghidersa & Dušek (2000). It consists of updating explicitly the nonlinear terms $\mathscr{N} = [(\boldsymbol{v} - \boldsymbol{u})\cdot\nabla]\boldsymbol{v}$ by a third-order Adams–Bashforth method and in solving the Stokes-like problem

$$\frac{\boldsymbol{v}^{(n+1)}}{\Delta t} + \nabla\cdot p^{(n+1)} + \frac{1}{G}\nabla^2\cdot\boldsymbol{v}^{(n+1)} = \frac{\boldsymbol{v}^{(n)}}{\Delta t} - \mathscr{N}, \tag{4.2a}$$

$$\nabla\cdot\boldsymbol{v}^{(n+1)} = 0, \tag{4.2b}$$

where Δt is the time step, $(n+1)$ the current time step and (n) the previous one. The boundary condition (2.3), taken at the same time, is:

$$\boldsymbol{v}^{(n+1)}|_S = \boldsymbol{u}^{(n+1)} + \boldsymbol{\Omega}^{(n+1)} \times \boldsymbol{r}|_S. \tag{4.3}$$

As explained above, the motion equations have to be discretized by an implicit scheme:

$$\frac{\rho_0}{\rho}\,\frac{\boldsymbol{u}^{(n+1)} - \boldsymbol{u}^{(n)}}{\Delta t} = \frac{6}{\pi}\,\boldsymbol{F}_{fl}\big(\boldsymbol{v}^{(n+1)}, p^{(n+1)}\big) - \boldsymbol{i}, \tag{4.4a}$$

$$\frac{\rho_0}{\rho}\,\frac{\boldsymbol{\Omega}^{(n+1)} - \boldsymbol{\Omega}^{(n)}}{\Delta t} = \frac{60}{\pi}\,\boldsymbol{M}_{fl}\left(\boldsymbol{v}^{(n+1)}, p^{(n+1)}\right), \tag{4.4b}$$

to accommodate light particles without loss of stability. The solving procedure described in Jenny & Dušek (2004) is based on the linearity of the Stokes-like problem (4.2) and on the linearity of the dependence of the hydrodynamic force (2.5) and torque (2.5) on the pressure and velocity fields. Let us consider a first guess $(\tilde{\boldsymbol{v}}, \tilde{p})$ for the flow field at the $(n+1)$th step obtained by solving (4.2) for known boundary conditions (4.3) at the previous (nth) step. The equations of motion (4.4) are rewritten introducing the residual $\boldsymbol{R} = [(6/\pi)\,\boldsymbol{F}_{fl}(\tilde{\boldsymbol{v}}, \tilde{p}) - \boldsymbol{i}, (60/\pi)\,\boldsymbol{M}_{fl}(\tilde{\boldsymbol{v}}, \tilde{p})]^T$ in the following way:

$$\frac{\rho_0}{\rho\,\Delta t}\boldsymbol{X} = \boldsymbol{R} + \boldsymbol{C}, \tag{4.5}$$

where $\boldsymbol{X}$ denotes the velocity correction $[\boldsymbol{u}^{(n+1)}-\boldsymbol{u}^{(n)}, \boldsymbol{\Omega}^{(n+1)}-\boldsymbol{\Omega}^{(n)}]^T$ and $\boldsymbol{C}$ the force correction $[(6/\pi)(\boldsymbol{F}_{fl}(\boldsymbol{v}^{(n+1)}, p^{(n+1)})-\boldsymbol{F}_{fl}(\tilde{\boldsymbol{v}}, \tilde{p})), (60/\pi)(\boldsymbol{M}_{fl}(\boldsymbol{v}^{(n+1)}, p^{(n+1)})-\boldsymbol{M}_{fl}(\tilde{\boldsymbol{v}}, \tilde{p}))]^T$ depending linearly on the flow field correction. Owing to the linear dependence of the Stokes problem (4.2) on the boundary condition (4.3), the term $\boldsymbol{C}$ can be expressed as $\boldsymbol{A}\,\boldsymbol{X}$, where $\boldsymbol{A}$ is a 6×6 matrix which depends only on the geometry, viscosity (G) and the time step Δt (see details in Jenny & Dušek 2004). It has rarely to be recomputed during a given simulation because the time step varies only in the initial stages of the vertical acceleration. The simple system of six linear equations

$$\left(\frac{\rho_0}{\rho\,\Delta t}\mathbf{1}-\boldsymbol{A}\right)\boldsymbol{X}=\boldsymbol{R}, \tag{4.6}$$

is easily solved to calculate the velocities $\boldsymbol{u}^{(n+1)}$ and $\boldsymbol{\Omega}^{(n+1)}$ and to update the boundary conditions (2.3) used to compute, finally, the flow field $(\boldsymbol{v}^{(n+1)}, p^{(n+1)})$.

The necessity of adopting the described implicit approach without splitting the force term on the right-hand side of (4.4*a*) is best clarified by reminding ourselves of the added mass effects (Mougin & Magnaudet 2002*a*). Matrix $\boldsymbol{A}$ includes both the added-mass and viscous effects. However, for $\Delta t\to 0$, the viscous effects vanish and the matrix becomes $\mathrm{diag}(C_{am}/\Delta t, C_{am}/\Delta t, C_{am}/\Delta t, 0, 0, 0)$ (see Jenny *et al.* 2003) where $C_{am}=0.5$ is the added mass coefficient for a sphere. The explicit way to solve the motion equations (2.4) would be to solve the system:

$$\boldsymbol{u}^{(n+1)}=\left(1-\frac{C_{am}}{\rho_0/\rho}\right)\boldsymbol{u}^{(n)}+\frac{C_{am}}{\rho_0/\rho}\boldsymbol{u}^{(n-1)}+\frac{\Delta t}{\rho_0/\rho}\hat{\boldsymbol{F}}, \tag{4.7}$$

where $\hat{\boldsymbol{F}}$ is the difference between the whole hydrodynamic force and the added-mass term. To analyse the numerical stability of (4.7), we consider $\Delta t\to 0$. In that case, the third term on the right-hand side vanishes and the sphere velocity is reduced to its vertical component u_z. Equation (4.7) reduces to:

$$u_z^{(n+1)}=(1-\alpha)u_z^{(n)}+\alpha u_z^{(n-1)}, \tag{4.8}$$

where α stands for $C_{am}/(\rho_0/\rho)$. This series requires two initial conditions $u_z^{(0)}$ and $u_z^{(-1)}$ yielding the closed form:

$$u_z^{(n)}=u_z^{(0)}-\frac{\Delta u_z^{(0)}\alpha}{1+\alpha}(1-(-\alpha)^n), \tag{4.9}$$

where $\Delta u_z^{(0)}=u_z^{(0)}-u_z^{(-1)}$ is proportional to an initial acceleration. It is obvious that the series has a limit for $n\to+\infty$ if and only if $\alpha<1$, i.e. when $\rho_0/\rho>C_{am}=0.5$. Extracting the added mass term from the motion equations (2.4) is an alternative way of avoiding numerical divergence for a light particle (see Mougin & Magnaudet 2002*a*).

In Jenny & Dušek (2004), two types of validation are presented. First, the numerical convergence of the discretization is demonstrated and, secondly, a validation by comparison to the experiment described in § 3 is presented in the oblique ascension regime for $\rho_0/\rho=0.89$ and $G=173$. The agreement in capturing the acceleration stage and the transition to the asymptotic regime was found to be very satisfactory.

5. Primary instability and a steady oblique ascension or fall

In the following sections, we present the dynamics of the system represented by the freely moving sphere and by the surrounding fluid in various transitional regimes.

After discretization, this system has many (of the order of 10^5) degrees of freedom relative to the description of the flow field plus 6 degrees of freedom describing the movement of the solid sphere. In spite of the many degrees of freedom, in the transitional domain, the dynamics remains that of a low-dimensional system and can be faithfully described by a single degree of freedom. Of course, during the simulations, all the 6 degrees of freedom of the sphere and the velocity field at several points of the wake were monitored confirming this claim. In what follows, we base the presentation on the description of the sphere motion in terms of the two horizontal velocity components.

5.1. *Linear theory*

In order to investigate the primary instability, the Navier–Stokes system is linearized about the axisymmetric solution. The azimuthal decomposition used in our code allows a direct linear analysis, which is the most accurate way to determine the threshold value of G. The immediate consequence of the axisymmetry and of the absence of swirl in the unperturbed flow is that the space on which the linearized Navier–Stokes operator is defined can be broken up into an orthogonal system of subspaces each associated to a given absolute value of the azimuthal wavenumber (Ghidersa & Dušek 2000). It is known (Natarajan & Acrivos 1993) that the most unstable subspace corresponds to the wavenumber $m = 1$. The degrees of freedom added to the system by the free motion of the sphere increase the dimension of the $m = 0$ subspace by two (vertical components of the translation and angular velocities) and that of the $m = 1$ subspace by four (horizontal components of the translation and angular velocity) (see Jenny *et al.* 2003). All the other subspaces remain unchanged and, as a consequence, only the stability of $m = 0, 1$ subspaces can change. The results of linear analysis show that the primary instability corresponds to a real eigenvalue associated to the $m = 1$ subspace for all density ratios ρ_0/ρ. (This implies a non-oscillating growth of small perturbations.) The additional degrees of freedom are responsible for a decrease of stability of the axisymmetric regime. This decrease is, however, not very significant. Instead of $G = 160$ ($Re_\infty = 212$) for $\rho_0/\rho \to \infty$ or a fixed sphere, the threshold moves down to $G = 155$ ($Re_\infty = 205$) for infinitely light spheres, $\rho_0/\rho = 0$ (Jenny *et al.* 2003). This can be partly explained by the strong similarity of the unstable eigenvectors for these extreme density ratios at the instability threshold (Jenny & Dušek 2004).

5.2. *Breaking of axisymmetry and plane oblique trajectories*

The spectral azimuthal decomposition implemented in the used code makes the axisymmetry of the base flow accurate. As a consequence, the (unstable) axisymmetric state has to be perturbed to trigger the instability. This can be done easily either by perturbing the sphere velocity in a well-defined direction at the initial condition or by adding small-amplitude noise in the initial stages of the simulation. The latter method was used for the simulating of whole trajectories of particles starting from rest. Whatever the method, the simulations confirm (see § 3 and Ghidersa & Dušek 2000) that a symmetry plane is selected by the initial conditions. A description of the movement of the sphere is presented in figure 4. They represent the trajectory of a light sphere with a density ratio 0.5 released at rest (figure 4*a*). This slightly supercritical trajectory ($G_{crit} = 156.1$) presents first a vertical acceleration (figure 4*c*) during which the axisymmetric state remains stable. Indeed, the random noise maintained until $t = 50$, visible in the logarithmic plot of the horizontal velocity (figure 4*b*), triggers no

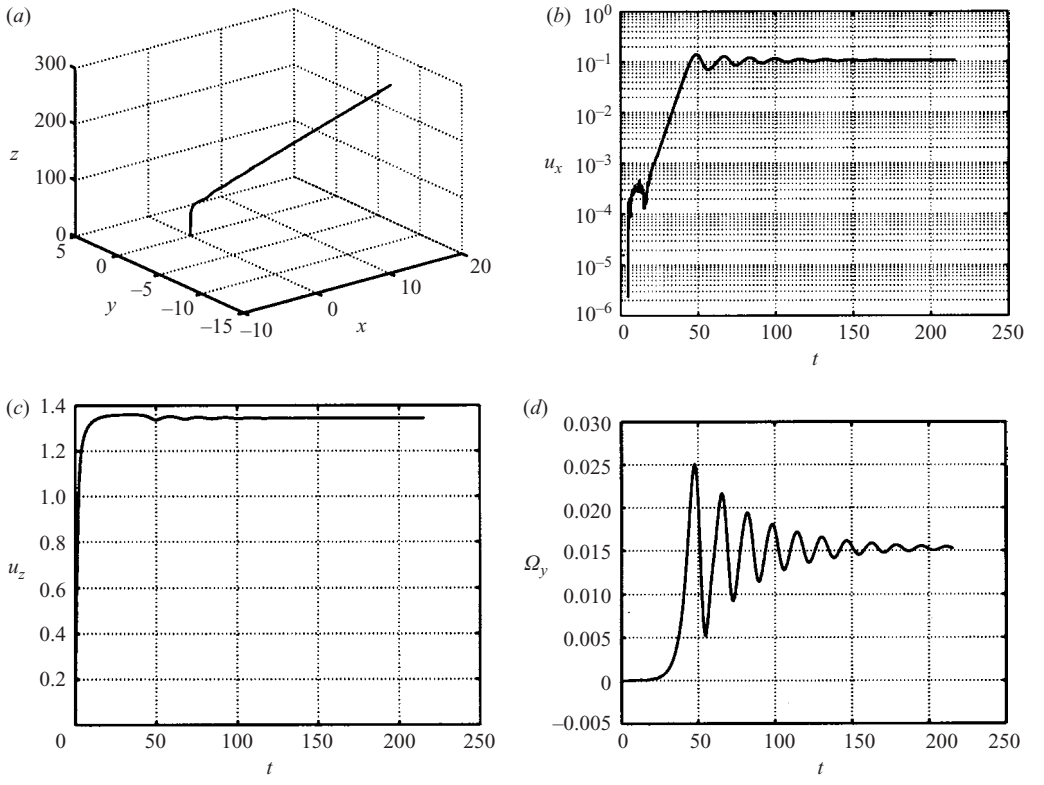

FIGURE 4. Acceleration from rest of a sphere of density ratio $\rho_0/\rho = 0.5$ at $G = 170$. (*a*) Trajectory. (*b*) Semi-logarithmic plot of the horizontal velocity u_x (x being the horizontal axis of the trajectory plane). (*c*) Vertical velocity. (*d*) Angular velocity (Ω_y, y being the axis normal to the plane). The plane of the trajectory corresponds to the symmetry plane of the wake.

exponential growth until $t \approx 20$. (The bump at $t \approx 15$ shows the random selection of the trajectory plane. Before emerging substantially from the imposed random noise, the direction of the horizontal velocity is constantly perturbed. At $t \approx 15$, its direction happens to be almost perpendicular to the final trajectory plane.) The instability sets in as soon as both a sufficient vertical velocity has been reached and a sufficiently long wake has developed at $t \approx 20$. As expected, the instability reduces the vertical velocity. The unstable mode is known to enhance the viscosity effects of (to 'pump' energy from) the base flow (Dušek, Fraunié & Le Gal 1994). The instability reduces the vertical velocity. The vanishing oscillations correspond to the next instability which makes the wake unsteady at higher G numbers and is due to a Hopf bifurcation, the threshold of which is at $G = 173.15$ for the density ratio $\rho_0/\rho = 0.5$ (see § 5.3 and table 1). The asymptotic state is steady. Note that the sphere rotates, albeit slowly, under the action of the torque resulting from the axisymmetry breaking (see figure 4*d*). The angular velocity vector of the rotation is normal to the plane of the trajectory. The rotation is not essential for the instability onset. Numerical experiments show that even if the rotation of the sphere is blocked, the asymptotic trajectory is not dramatically modified and the primary instability threshold moves only slightly upward in terms of G.

ρ_0/ρ	G_-	λ_1	G_+	λ_2	$G_{2,crit}$	$Re_{2,crit}$	f	St	C_i/C_r
0	165	-3.2×10^{-2}	170	5.2×10^{-2}	166.9	224.1	0.068	0.051	1.15
0.5	170	-2.4×10^{-2}	175	1.4×10^{-2}	173.2	234.9	0.065	0.048	2.33
0.89	175	-1.1×10^{-2}	180	8.2×10^{-3}	177.9	242.4	0.067	0.049	–
1.3	180	-2.0×10^{-2}	190	2.0×10^{-2}	185	254.8	0.070	0.051	$\sim$1.7
2	190	-3.1×10^{-3}	195	7.1×10^{-3}	191.5	266.1	0.075	0.054	$\sim$1.4
3	190	-3.1×10^{-2}	195	4.6×10^{-3}	194.4	271.1	0.176	0.126	–
5	190	-5.0×10^{-2}	195	5.9×10^{-3}	194.5	271.6	0.176	0.126	–
∞					195.7	274	0.178	0.127	-0.47

TABLE 1. Variation of the threshold value of the Hopf secondary bifurcation. ($G_\pm$, Galileo numbers, respectively, below and above the instability, threshold, $\lambda_\pm$ corresponding amplification rates, $G_{2,crit}$ interpolated critical Galileo number for the secondary instability threshold, $Re_{2,crit} = \langle U\rangle_\infty G_{2,crit}$. f is the frequency and the Strouhal number is defined as $St = f/\langle U\rangle_\infty$. The constant of the Landau model $C_i/C_r = (\omega_i - \omega_\infty)/\lambda$ where ω_i and ω_∞ are, respectively, the angular frequency of the linear and saturating oscillations. It has not been determined in cases marked '–'.

5.3. *Azimuthal modes – nonlinear modes of the axisymmetry breaking instability*

In Ghidersa & Dušek (2000), it is shown that the azimuthal decomposition series which described the wake of a fixed sphere converges with only a few modes taken into account ($0 < m < 4$). Indeed, the maximum amplitude of the modes decreased by about one decade from mode m to $m+1$ at $Re = 250$. This is because the $m > 1$ azimuthal modes are, in fact, higher-order nonlinear modes behaving roughly in proportion to the instability amplitude to the power of m. As a result, not very far from the instability threshold, the convergence is extremely fast. As shown by numerical testing in Jenny & Dušek (2004), a similar convergence holds for a free sphere, moreover the convergence appears to be very good in the whole transition domain.

Figure 5 shows differences with respect to the fixed sphere wake of Ghidersa & Dušek (2000). The azimuthal modes of the wake of a free sphere do not decrease as fast as that of a fixed sphere for increasing azimuthal wavenumber. The distance between the crest of the modes and the axis is larger because the velocity of the free sphere is not parallel to the z-axis (figure 6). This purely geometric effect also enhances higher-order modes, especially in the far wake. Close to the sphere, the wake is, however, accurately described using only 7 azimuthal modes ($m = 0$ to $m = 6$) and the accuracy of the resulting direct numerical simulations is better than 1% (see Jenny & Dušek 2004) even for highly supercritical regimes with a restricted number of modes. Figure 5(c) shows that the amplitude of the last mode ($m = 6$) is negligible for $z < 10$ diameters. Of course, in the far wake, the convergence is slower. Although the far wake has no effect on the sphere motion, it is necessary to take enough azimuthal modes because insufficient azimuthal resolution causes numerical instabilities at the lateral boundary of the computational domain. The 7 modes mentioned were, nevertheless, quite enough for this purpose.

5.4. *Absence of bifid wake*

The analysis of the flow in the wake of the light sphere of density ratio 0.5 at $G = 170$ reveals another striking difference as compared to the fixed sphere wake. The latter is known to present a characteristic 'bifid' structure in flow visualization. In Ghidersa & Dušek (2000) this phenomenon has been explained in terms of the superimposition of

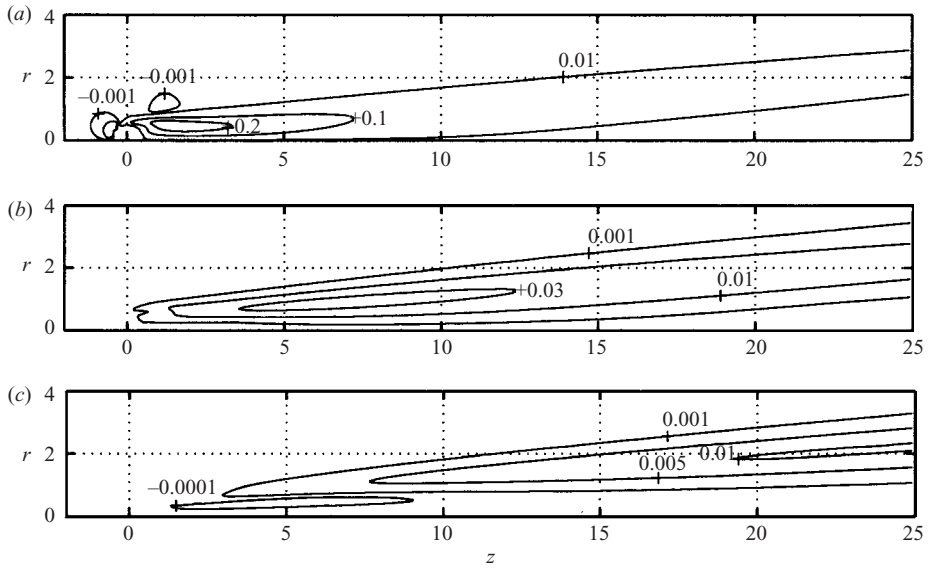

FIGURE 5. Iso-values of the azimuthal modes of the axial velocity at $G = 170$ and $\rho_0/\rho = 0.5$. The value of the velocity component represented is the (real) value obtained after rotating the modes into the symmetry plane. (*a*) Mode $m = 1$, $max = 0.274$ at $r = 0.5$ and $z = 1.5$. (*b*) Mode $m = 3$, $max = 0.037$ at $r = 0.9$ and $z = 6.7$. (*c*) Mode $m = 6$, $max = 0.010$ at $r = 2.1$ and $z = 23.2$.

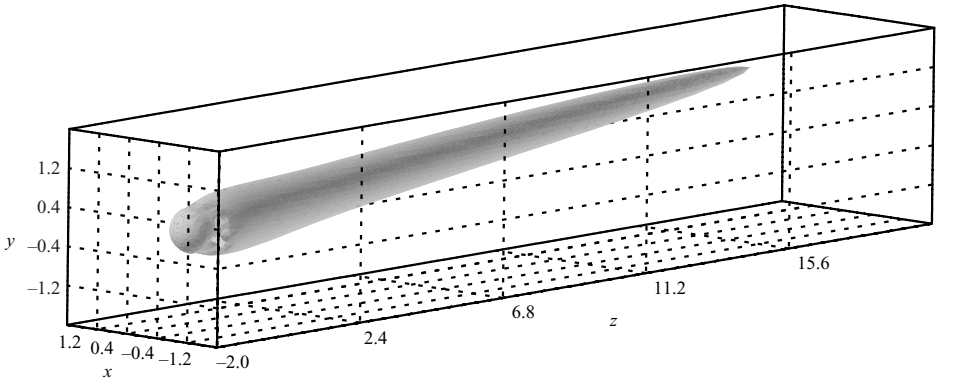

FIGURE 6. Iso-surface of the axial velocity $v_z = -0.27$ at $G = 170$ and $\rho_0/\rho = 0.5$. The velocity of the fluid entrained by the sphere is oriented upward. The projection onto the z-axis of the moving frame is thus negative (see figure 3).

the axisymmetric flow and of the fundamental instability mode. The latter comprises two counter-rotating vortices always visible on iso-vorticity plots (see Thompson, Leweke & Provansal 2001). If, however, the axisymmetric transverse flow dominates locally over the axisymmetry breaking perturbation, the vortices do not emerge. The profiles of the fundamental instability mode for a light sphere is different to that for a fixed sphere and its streamwise decay is rather fast along the flow axis (see figure 5*a*). As a result, the streamwise vortices never appear in the flow cross-sections of figure 7. Both close to the sphere (at $z = 3$ diameters) and far downstream ($z = 15$) the cross-sections are similar to what can be seen in the domain of a single wake for a fixed sphere, i.e. only a deformation of the axisymmetric pattern with just one

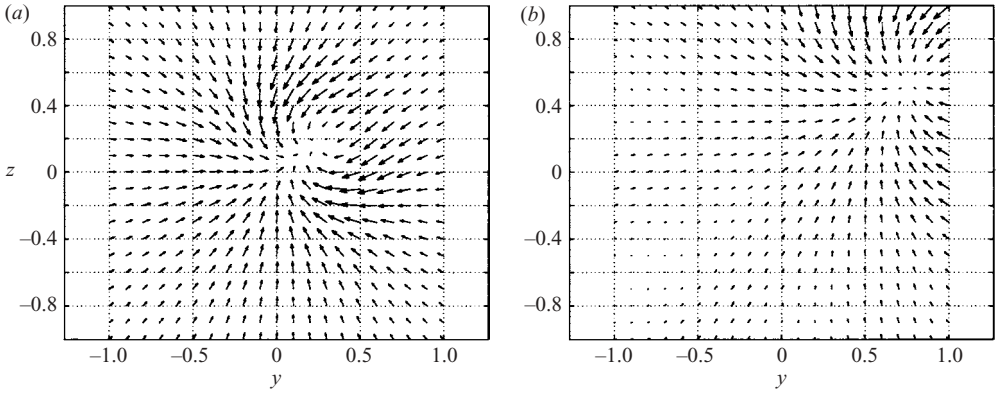

FIGURE 7. Transverse flow at $z = 3$ and $z = 15$ diameters downstream of the sphere centre for a light sphere ($\rho_0/\rho = 0.5$ at $G = 170$ (steady oblique regime).

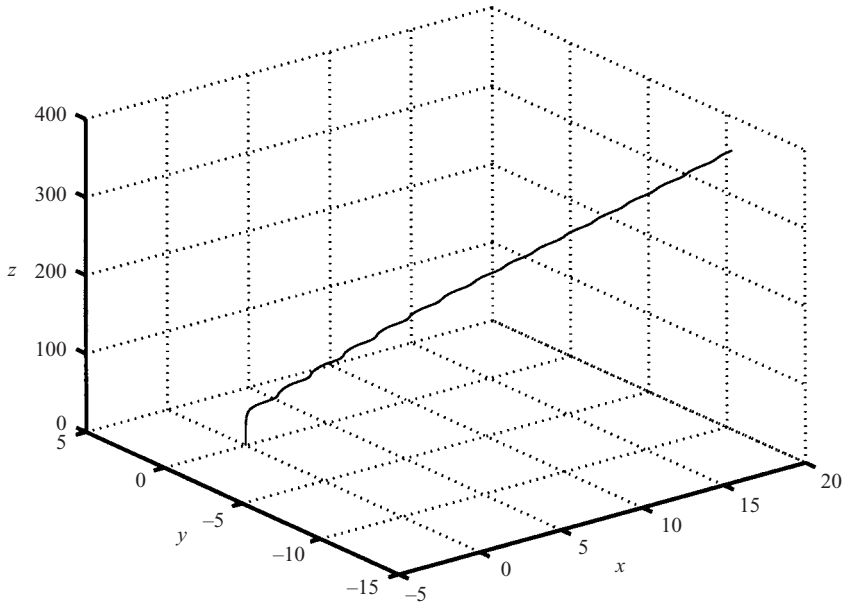

FIGURE 8. Trajectory of a free ascending sphere on a plane fixed by initial perturbations at $G = 170$ and $\rho_0/\rho = 0$.

point of convergence. As a consequence, a dye injected at the sphere surface would concentrate in only one filament.

6. Transition to unsteadiness

6.1. *Onset of wavy oblique trajectories*

For all values of the density ratio, the steady oblique regime becomes unstable and gives way to unsteadiness. This unsteadiness corresponds to periodic oscillations of the sphere about an oblique mean direction. The trajectory remains in the same plane as the previously steady motion (figure 8). The frequency of the oscillations

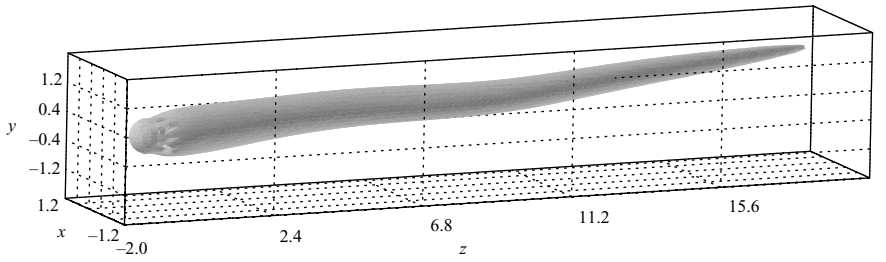

FIGURE 9. Oscillating wake of a freely ascending sphere in the asymptotic state at $G = 170$ and $\rho_0/\rho = 0$. The wavelength is $\lambda = 13.2$.

is significantly lower than in a fixed sphere wake. For example, for $\rho_0/\rho = 0$ and at $G = 165$ the non-dimensional frequency is $f = 0.068$ $(T^*)^{-1}$ (see (2.1)). In terms of Strouhal number, defined as $St = f/U_\infty$, this corresponds to $St = 0.051$, a value considerably smaller than $St = 0.127$ found for the fixed sphere wake in Ghidersa & Dušek (2000). This feature appears to be characteristic of spheres with density ratio lower than 2.5.

The time period T of the sphere oscillations is related to a wavelength λ observable in figure 9. The wavelength is about 13.2 diameters which yields a phase velocity $c = \lambda/T$, calculated using the time period of the sphere velocity $(1/T = 0.068)$, of $c \approx 0.9$. This is in a very good agreement with other cases of von Kármán vortex streets such as in the cylinder wake of Williamson (1989) or in the wake of a fixed sphere (Ghidersa & Dušek 2000).

The Hopf bifurcation, which is at the origin of the unsteadiness, obeys very well the Landau model (Dušek *et al.* 1994) (see figure 10 for $\rho_0/\rho = 0.5$, $G = 175$ and figure 11 for $\rho_0/\rho = 0$, $G = 170$). It is of supercritical character which enabled us to calculate the critical Galileo number by interpolating between two amplification rates below and above the instability threshold (see table 1). The variation of the frequency due to nonlinear effects of the instability development has also been plotted. Unlike the known cases of the cylinder wake (see Sreenivasan, Strykowski & Olinger 1987; Dušek *et al.* 1994) or of the fixed sphere wake (see Ghidersa & Dušek 2000) the frequency shift is negative. Let us consider the normalized Landau constant (the ratio of the real and imaginary part of the coefficent of the nonlinear term of the Landau model) $\ell = -\Delta\omega/\gamma$ where $\Delta\omega$ is the difference of angular frequency of oscillations at the saturation and in the linear regime and γ is the linear amplification rate (for more details see e.g. Dušek *et al.* 1994). The latter was reported to be about -3 for the cylinder wake and -0.5 for a fixed sphere wake in the cited papers. The value found for a fixed sphere was also confirmed by Thompson *et al.* (2001). Figure 11(*c*) shows that the Landau constant is positive. The amplification rate from figures 10 and 11(*b*) combined with the angular frequency shift of figures 10 and 11(*c*) yields $\ell = 2.33$ for $\rho_0/\rho = 0.5$ and $\ell = 1.15$ for an infinitely light sphere. The figures show the difficulties in extracting the Landau constant from the simulations. It is necessary to capture a sufficiently long linear regime, i.e. to be sufficiently close to the instability threshold and have a weakly perturbed initial condition. These requirements have been met in figures 11(*c*) and the accuracy of the frequency shift and of the linear apmlification rates yield an error of less than 5% of the Landau constant value. This implies that the Landau constant varies significantly with varying density ratio, but is systematically positive for density ratios less than 2.5 (see table 1).

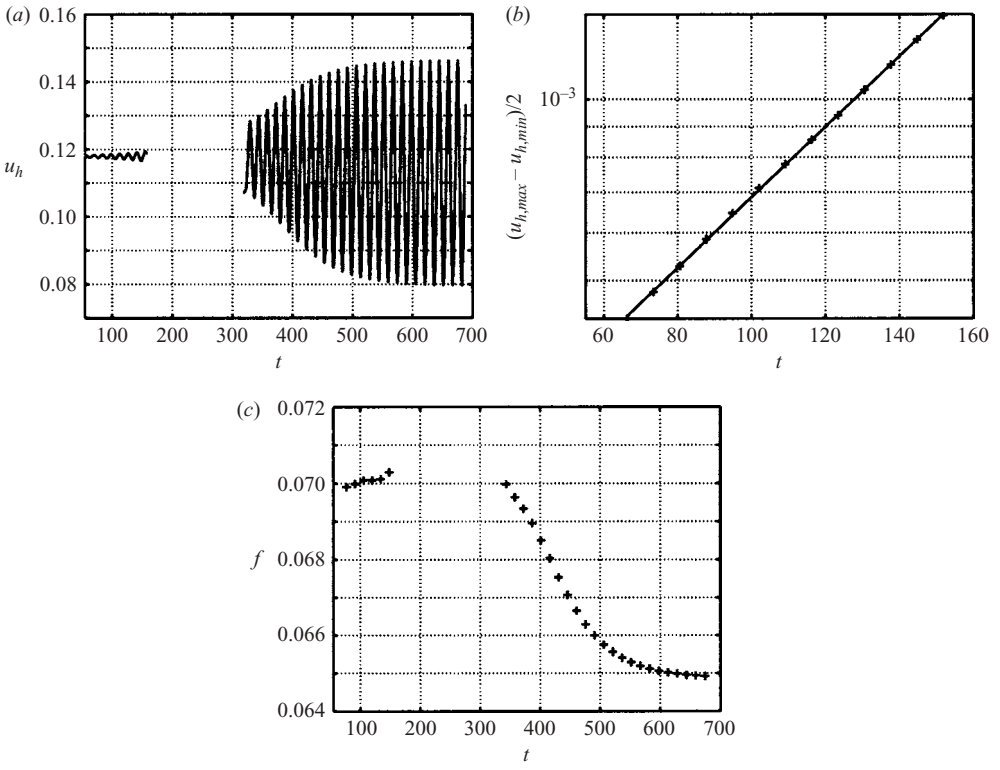

FIGURE 10. Development of unsteadiness at $G = 175$ and $\rho_0/\rho_f = 0.5$. (*a*) Only a small part of the linear amplification of a weak initial perturbation has been computed. (*b*) The linear amplification rate of the oscillation amplitude is $\gamma = 0.0135$. (*c*) Variation of the oscillation frequency.

6.2. *Role of density*

Obviously, in the unsteady regime, the density effects become more significant. Table 1 shows amplification rates computed for 8 different density ratios just below and above the secondary instability threshold. The critical Galileo number and its Reynolds number equivalent ($Re_{2,crit} = U_\infty G_{2,crit}$, U_∞ being the asymptotic velocity magnitude of the steady oblique regime losing its stability) are presented in the next two columns. The threshold values are calculated by linear interpolation. The dependence of the secondary instability threshold on the density is more significant than that of the primary one (figure 12). This can be explained by a greater influence of the accelerations on the left-hand sides of the motion equations (2.4*a*) and (2.4*b*). In this case, the acceleration is non-zero even in the asymptotic regime and is obviously greater in all stages of the secondary instability development than during the development of the primary instability.

Note that a variation of the density ratio brings about a significant change in the frequency of the periodic regime. Table 1 shows that the variation between the extreme cases of infinitely light and infinitely dense spheres (respectively, $f = 0.068$ and $f = 0.178$) is not uniform. For the density ratio $\rho_0/\rho = 2$, roughly the same frequency as for $\rho_0/\rho = 0$ characterizes the limit cycle. For the value of 3, the oscillations frequency changes to the value characteristic of dense spheres. At $\rho_0/\rho = 2$ and $\rho_0/\rho = 3$, the two frequencies appear to coexist during a long transitional time. This

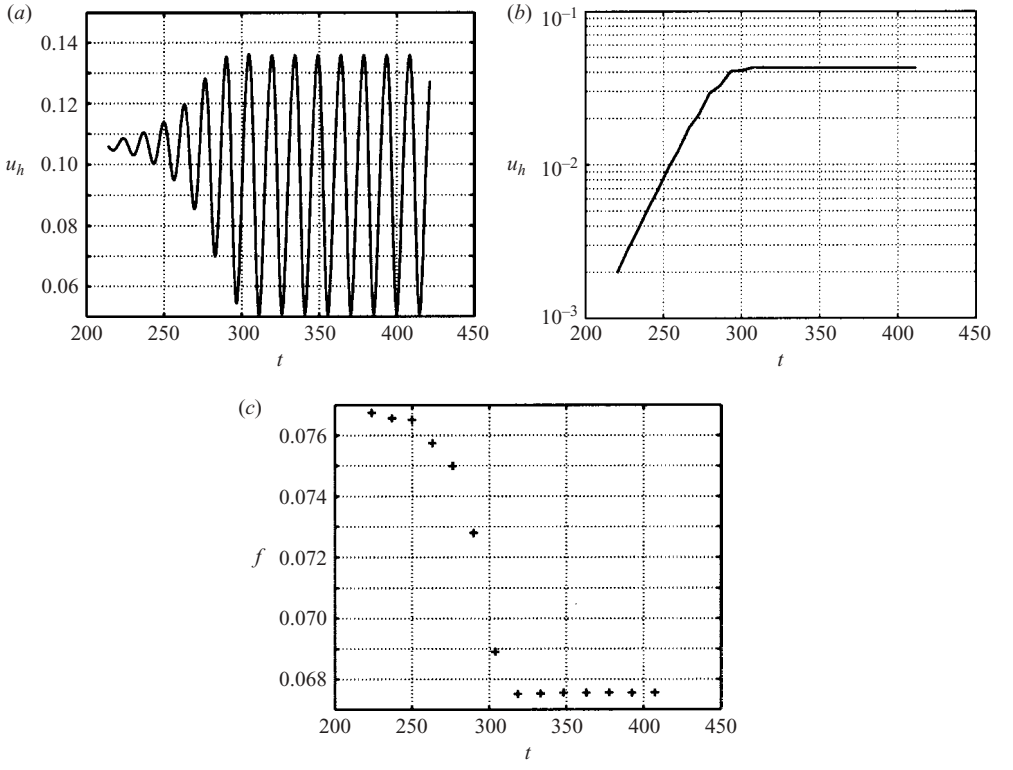

FIGURE 11. Development of the secondary instability at $G = 170$ and $\rho_0/\rho = 0$. (*a*) Oscillation amplitude of the magnitude of the horizontal component of the sphere velocity growing to saturation. (*b*) Semilogarithmic plot of the variation of the oscillation amplitude. The linear amplification rate is 0.052. (*c*) Variation of the frequency due to the saturation of the oscillation amplitude.

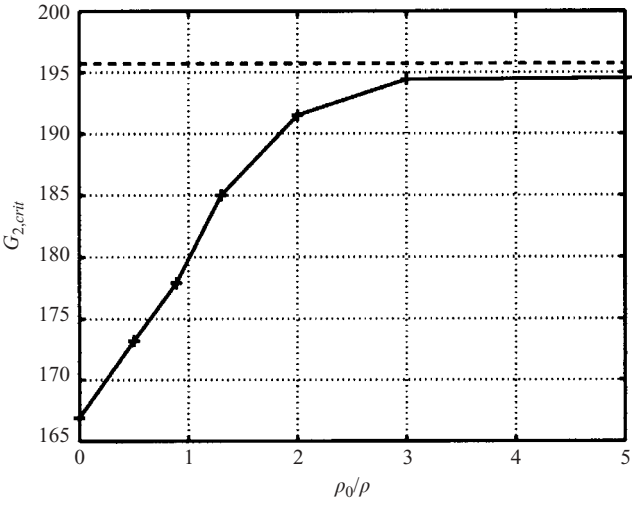

FIGURE 12. Critical values of Galileo number at the onset of the Hopf secondary bifurcation *vs.* the sphere density.

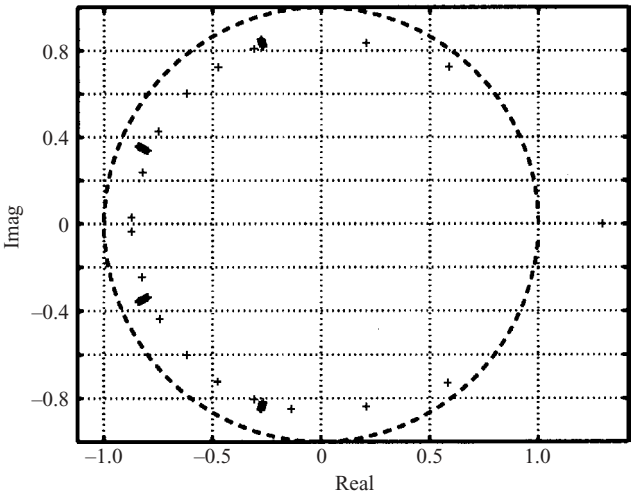

FIGURE 13. Most unstable eigenvalues of the linearized operator of the discretized problem at $G = 175$ and $\rho_0/\rho = 0.5$. The figure represents the real and the imaginary part of $\exp(\lambda_i)$ where λ_i is the complex eigenvalue number i. The stable eigenvalues are inside the circle of radius 1.

suggests that the limit value separating the lower- and higher-frequency domain is close to 2.5. This is in good agreement with Mordant & Pinton (2000) who observed experimentally a similarly low frequency ($f = 0.079$) at $G = 223$ and $\rho_0/\rho = 2.56$. The coexistence of both frequencies observed on both sides of the limit value implies that two pairs of complex eigenvalues, one with a smaller the other with a greater imaginary part, exist in the spectrum of the operator linearized with respect to the steady oblique state. At $\rho_0/\rho \approx 2.5$, both eigen-pairs are equally unstable, for lower density ratios the lower-frequency eigen-pair is more unstable and vice versa for higher density ratios.

6.3. *Strongly nonlinear effects of the primary instability*

It is numerically difficult to obtain the eigenvalues corresponding to the fully three-dimensional flow of the steady oblique regime. However, in Natarajan & Acrivos (1993), the eigenvalue analysis of the axisymmetric flow provides good information on the secondary (Hopf) bifurcation of the fixed sphere wake. For this reason, we analysed the eigenvalues of the operator linearized with respect to the axisymmetric state described in § 5. The 100 least stable eigenvalues in the (least stable) $m = 1$ subspace are presented in figure 13. Both for computational reasons and for the sake of clarity, it is preferable to compute the eigenvalues of the exponential of the operator. Figure 13 represents thus the exponentials e^{λ} for the density ratio 0.5 at $G = 175$, i.e. above the secondary instability threshold. The result is, this time, negative; no useful direct information on the secondary instability can be drawn from this analysis. First, no complex eigen-pair is outside the unit circle delimiting the stability region. Secondly, the eigen-pair closest to the circle becomes, indeed, unstable at higher values of G (at $G = 220$), but its angle with the real axis (corresponding to the angular frequency) is 0.88 radians; this yields the frequency $f = 0.14$ close to that typical for dense spheres. This allows us to conclude that the primary instability influences in an essential way the characteristics of the secondary instability.

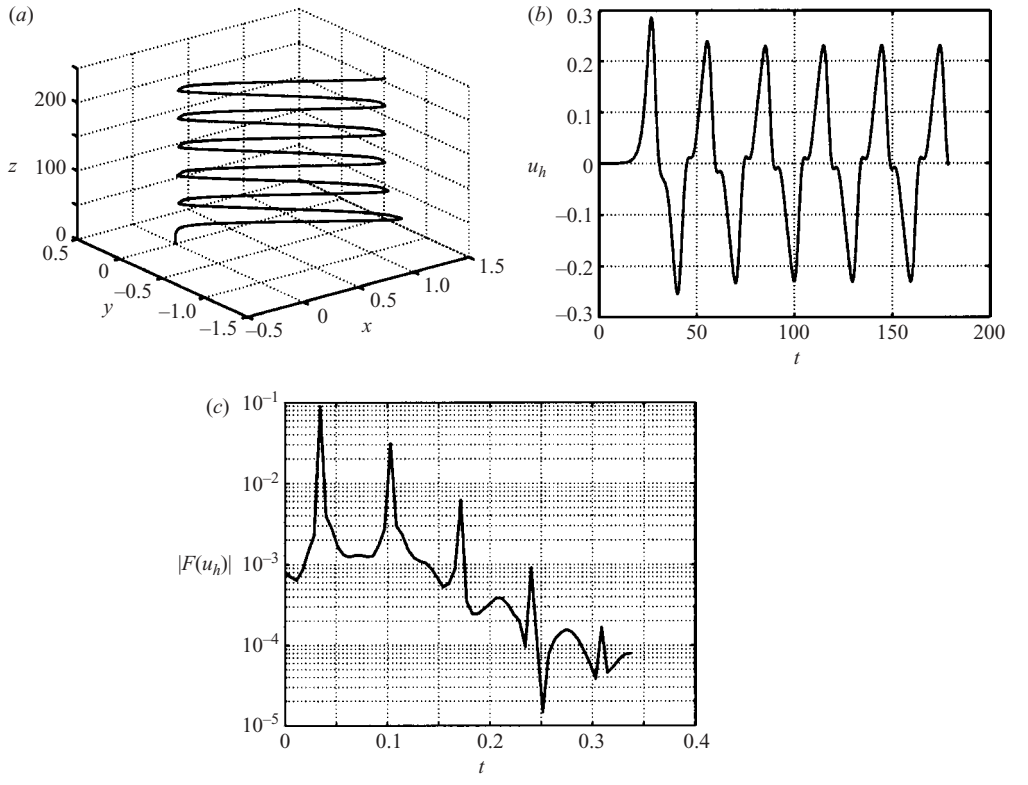

FIGURE 14. (*a*) Zigzagging trajectory of a sphere at $G = 200$ and $\rho_s/\rho_f = 0.5$. (*b*) Horizontal velocity component of the zigzagging motion of (*a*). (*c*) Fourier transform (spectrum) of the asymptotic regime (fundamental frequency $f = 0.0343$).

7. Subharmonic transition

7.1. *Results of simulation: observations*

For light spheres, the oblique periodic regime loses its stability very rapidly and gives way to trajectories of a different type (figure 14*a*). The figure represents a trajectory of a sphere of density ratio 0.5 released with a zero velocity. After a short initial vertical acceleration, the sphere deviates because of the onset of the primary instability, but there is no visible transient corresponding to an oblique wavy ascension. Instead, the trajectory rises vertically on average. The motion is periodic with a considerably longer period and the trajectory remains plane. As observed in § 1, such zigzagging trajectories are characteristic of spherical bubbles in not absolutely pure water (Wu & Gharib 2002), i.e. of bubbles behaving like light solid spheres. A more detailed investigation of the transition from the oblique wavy motion to the zigzagging motion shows that the regime represented in figure 14 is already rather strongly supercritical, the threshold of its onset lying below $G = 180$ for the considered density ratio of 0.5. This explains that the transients are very short and result merely in a shift of the mean vertical line with respect to the origin of the trajectory. Figure 14(*b*) shows a strongly unharmonic character of the oscillations with a 'hesitation' in the vertical ascension stages. The most striking features of the Fourier analysis of the periodic asymptotic regime is the absence of pair harmonics and the abnormally strong third harmonic. As a rule, the higher-order harmonics are proportional to the power of the

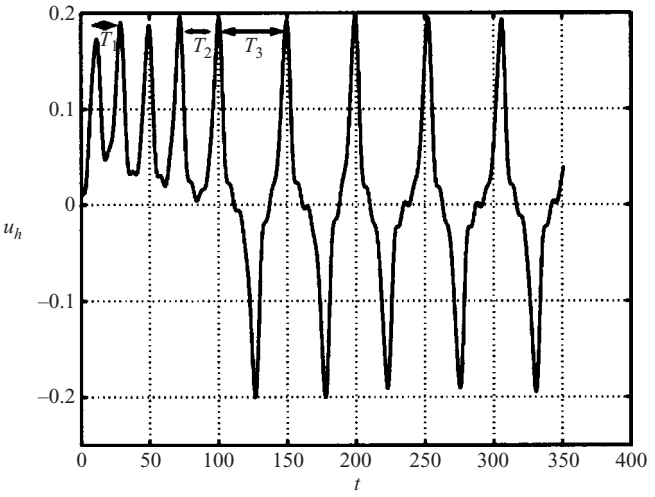

FIGURE 15. Onset of the zigzagging motion at $G = 180$, i.e. close to the threshold of this regime for a sphere of density ratio $\rho_0/\rho = 0.5$. $T_1 = 17.35$, $T_2 = 28.37$, $T_3 = 49.35$.

fundamental one, the exponent being equal to the order of the harmonic (see Dušek *et al.* 1994). This would yield a pure exponential decay.

To see how the zigzagging trajectory arises, it is preferable to choose a slightly supercritical regime such as that in figure 15. The initial condition of the simulation is that of an established wavy oblique asymptotic state obtained at $G = 175$ with the same density ratio of 0.5. The horizontal velocity presents a growing amplitude. At the same time, the period of oscillations grows too, manifestly due to a 'hesitation' when the trajectory approaches a vertical direction, i.e. when the horizontal velocity approaches zero. As soon as the vertical direction is reached, the trajectory does not go back to the initial half-plane, but the next period continues in the opposite half-plane (the velocity curve has the same form, but has the opposite sign in the next period). The toggling of the deviation brings about a period doubling. The initial increase of period in figure 15 is close to a factor of 1.5 ($T_2/T_1 \approx 1.6$). T_3/T_2 is, indeed, almost 2 (1.74) which yields, as a result, not a period doubling but a period tripling. Figure 16 confirms that this observation is neither an artefact due to the transients appearing when the parameter G changes nor a coincidence occurring for a single density ratio. The notion of subharmonic transition refers to asymptotic states. For this purpose, figure 16 presents three asymptotic states at $G = 180$, $G = 192$ and $G = 200$ for a sphere of density ratio $\rho_0/\rho = 0.89$. The value $G = 180$ in figure 16(a) lies only slightly above the threshold of the wavy oblique regime. $G = 192$ (figure 16b) is slightly below the onset of zigzagging and $G = 200$ (figure 16c) corresponds to the zigzagging regime. The period in figure 16(c) is about 2.5 times longer than in figure 16(a) and the trend of the period to increase at the approach of the change of the regime (figure 16b) is obvious. The fact that the ratio of the periods in figures 16(c) and 16(a) is not three can be explained by a rather rapid decrease of period with growing G above the threshold of zigzagging.

7.2. *Theoretical analysis*

The period tripling can be related to the absence of pair harmonics of the velocity oscillations stated in figure 14(c). The absence of pair harmonics itself can easily be explained on the basis of the following symmetry argument.

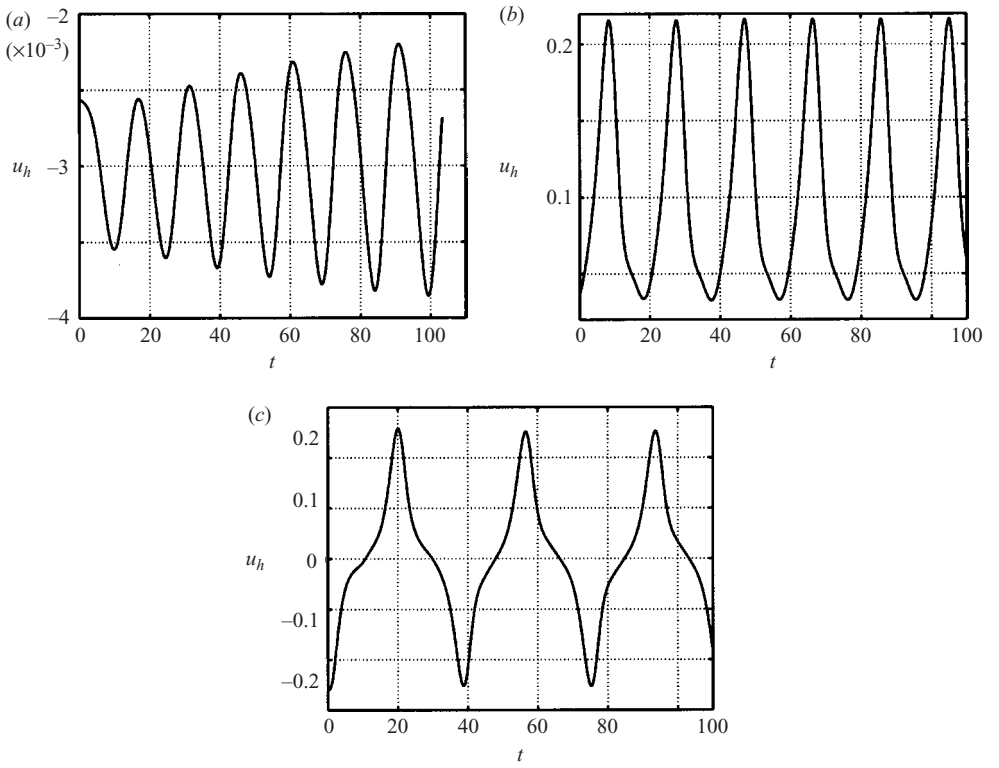

FIGURE 16. $\rho_0/\rho = 0.89$. (*a*) $G = 180$, $T = 14.82$. (*b*) $G = 192$, $T = 19.33$. (*c*) $G = 200$, $T = 36.78$.

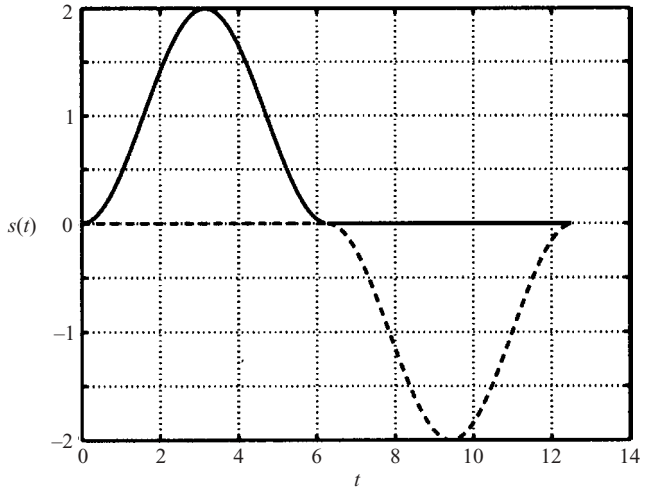

FIGURE 17. Toggling sinusoidal oscillations modelled by the function: $s(t) = (-1)^{[t/2\pi]}\,[1 - \cos(t)]$ ([x] meaning the truncation to the nearest lower integer.)

Figure 17 helps us to understand that the toggling of the trajectory about the vertical direction amounts to the following symmetry condition for the horizontal velocity u_h (projection of the sphere velocity onto the horizontal axis in the plane of

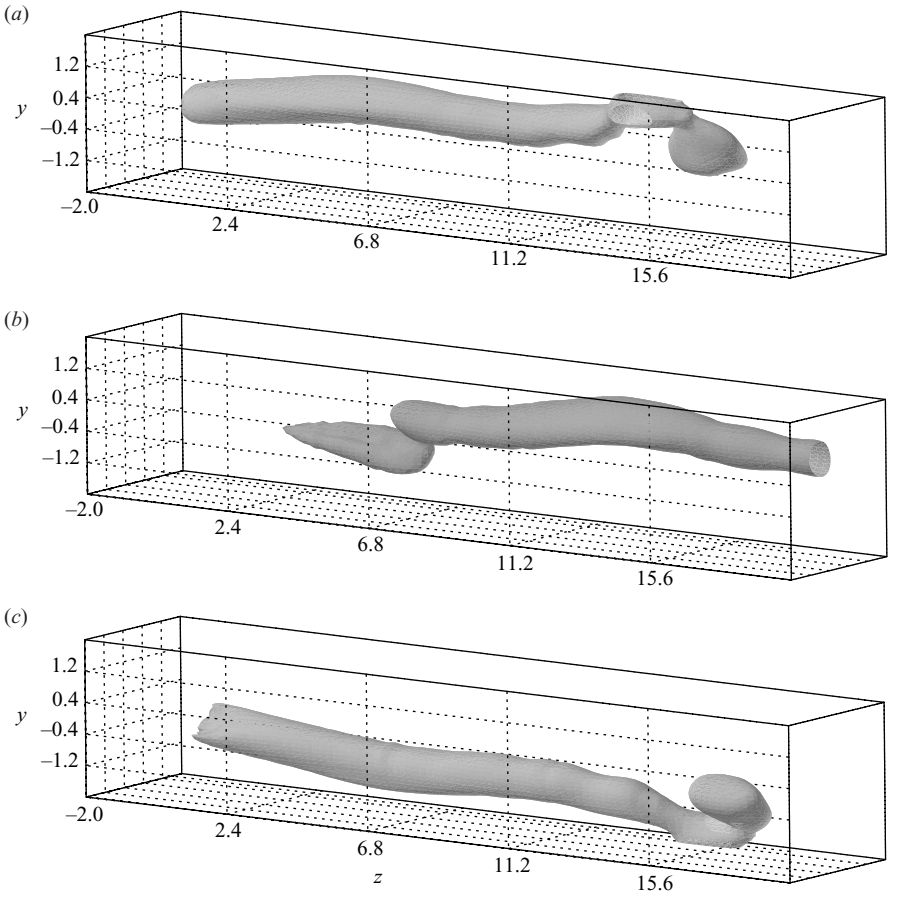

FIGURE 18. Isosurface $v_z' = -0.12$ of the non-axisymmetric perturbation (sum of all azimuthal modes except $m = 0$) of the wake of an ascending sphere of density ratio $\rho_0/\rho = 0.5$ at $G = 200$. (*a*) $t = 0$: Maximal amplitude of the horizontal velocity in one direction. (*b*) $t = T/4 = 7.263$: Stage of vertical ascension. (Note the absence of perturbation implying axisymmetry in the near wake.) (*c*) $t = T/2 = 14.527$: Maximal amplitude of horizontal velocity in the opposite direction.

the trajectory):

$$u_h(t + T/2) = -u_h(t), \tag{7.1}$$

where T is the period of the zigzagging motion. The coefficients of the Fourier series:

$$u_h(t) = \sum_{n=-\infty}^{+\infty} c_n \exp\left(\mathrm{i}\frac{2\pi}{T}nt\right), \tag{7.2}$$

thus satisfy

$$c_n = (-1)^{n+1} c_n. \tag{7.3}$$

In the absence of the second harmonic, the simplest ratio for a subharmonic transition is 3, in other words, the primary frequency (triggered by the secondary instability) excites the third harmonic of the zigzagging motion. To adapt to this period tripling, the period has to increase by 50% before doubling via the toggling mechanism. The reason for the toggling is clarified by figure 18, representing the wake of the sphere

the trajectory of which was presented in figure 14. The figure represents the isosurface corresponding to a level of the perturbation of the vertical velocity $v_z' = -0.12$, the mean vertical velocity of the sphere being 1.38. The negative value means that the perturbation enhances the entrainment of the fluid; note that the vertical z-axis is placed horizontally and points downstream. Three stages of a period of the zigzagging motion are represented. It appears that, whenever the trajectory reaches the maximum excursion from the vertical line, the near wake becomes axisymmetric, i.e. the lift force and the torque temporarily disappear. As a consequence, the horizontal acceleration is zero (and not maximal, the rotation stops). This not only explains the 'hesitation' in this stage, but it implies that the sphere crosses to the opposite half-plane by inertia of the wake, presenting a flapping motion. The periodic extinction allows the perturbation to be recreated identically on both sides of the vertical line.

8. Loss of planar symmetry, chaos

8.1. *Chaotic trajectories and flow field*

We have seen that the periodic regimes of light and heavy spheres are different. The light spheres, unlike the heavy ones, undergo a subharmonic bifurcation and reach a zigzagging regime. As G increases, the sphere trajectory becomes chaotic, whatever the density ratio. The transition to chaos occurs from the zigzagging regime for light spheres and from the oblique oscillating regime for heavy spheres. The onset of chaos coincides with the breaking of the planar symmetry of the wake. The chaotic trajectories are fully three-dimensional (see figures 19 and 20).

The mean value of the horizontal velocity tends to zero and the trajectory is vertical on average. The trajectory in figure 20(a) resembles strongly a helical one, but as can be seen in figure 20(b), the velocity is chaotic. The spectra (absolute values of the Fourier transforms) in figures 19(c) and 20(c) present the typical 'continuous' aspect characteristic of chaotic signals. In figure 20(c), no dominant frequency appears. The highest peak in figure 19(c) corresponds to the frequency $f \approx 0.14$. This value may be regarded as a second harmonic of the frequency of the secondary bifurcation ($f = 0.068$, see § 6). However, in the spectra characterizing the chaotic dynamics (see § 8.3) for light spheres, the low frequency ($f = 0.07$) is never observed, whereas the higher one is omnipresent. The linear anlysis of the unstable axisymmetric state at Galileo numbers corresponding to chaotic regimes shows that the rightmost eigenvalue pair e^{λ} in figure 13 has become unstable (in addition to the already unstable real value). Note that the argument of e^{λ} (manifestly a little smaller than $\pi/3$ in figure 13) corresponds to the imaginary part of λ, i.e. $2\pi \times 0.14 \approx 0.88$. This suggests that the primary instability is destroyed and the linear analysis of the axisymmetric wake partly regains a qualitative relevance. It might also explain the quasi-helical trajectory in figure 20(a) because helical modes represent unsteady axisymmetry breaking modes.

The instantaneous flow field presents, naturally, a spatially chaotic structure and has no longer any symmetry (figure 21). In the near wake, because the chaotic flow is the result of a transition triggered originally by the axisymmetry breaking bifurcation, the chaotic structures are better represented by iso-surfaces of the non-axisymmetric part of the flow field obtained by summing all azimuthal modes except the axisymmetric one (modes $m \geqslant 1$). Downstream of about $5d$, the chaotic structures completely dominate and the flow pattern appears even if the axisymmetric mode is included.

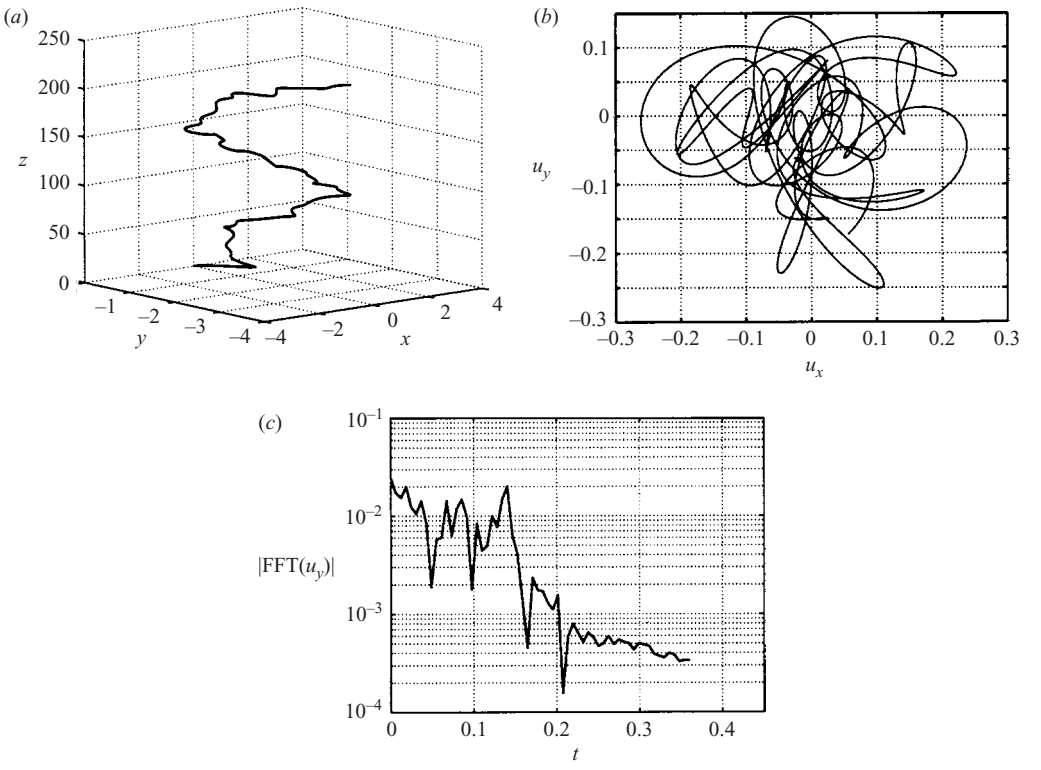

FIGURE 19. (*a*) Trajectory, (*b*) projection of the velocity vector onto the horizontal plane and (*c*) the modulus of the Fourier transform (spectrum) of u_y for an infinitely light sphere ($\rho_0/\rho = 0$) at $G = 210$.

8.2. *Onset of chaos*

To explain how the chaotic behaviour arises, we have to focus on the dynamics close to the threshold of its onset. Figure 22 show an exponential relaxation (figure 22*b*) of the three-dimensionality below a threshold (lying at $G \approx 218$) and an exponential growth (figure 22*e*) above this threshold. The simulation in figures 22(*a*)–(*c*) has the developed supercritical chaotic state for the initial condition. There is reversibility for increasing and decreasing Galileo numbers. A supercritical bifurcation thus seems to be responsible for the onset of the three-dimensionality of the trajectories. Figures 22(*a*) and (*b*) show a monotonous decay and figures 22(*d*) and (*e*) a monotonous growth. In other words, the perturbation is non-oscillating, i.e. the eigenvalue becoming unstable and responsible for the bifurcation is real, i.e. the bifurcation is regular. Figures 22(*c*) and 22(*f*) allow us to compare the oscillations in the subcritical (periodic) state and in the supercritical state. It appears clear that even before becoming completely chaotic and three-dimensional, the supercritical state presents a much slower dominant frequency of the horizontal velocity than the subcritical state (figure 22*g*). This frequency disappears when the initially supercritical trajectory converges to the periodic state. The frequency of the periodic state is $f = 0.18$. The dominant frequencies of the supercritical state are visible in figure 22(*g*). The slow frequency in figure 22(*f*) corresponds to the highest peak, at $f' = 0.05$. Two other peaks, at $f = 0.18$ and at $f - f' = 0.13$, dominate the spectrum.

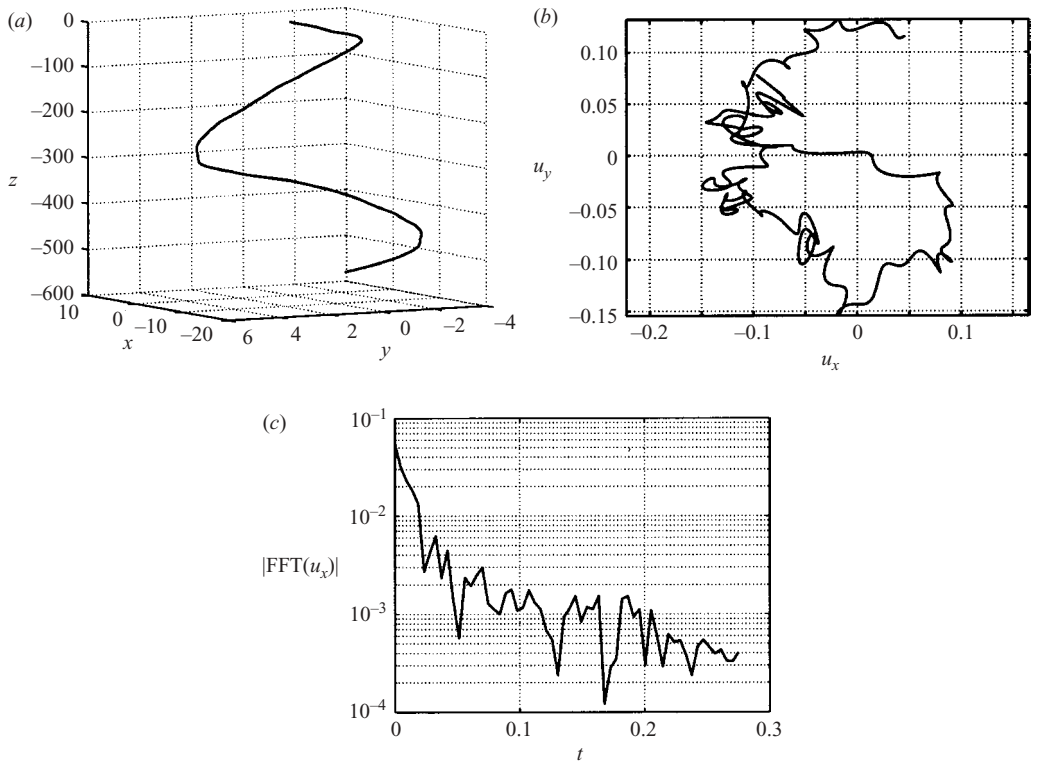

FIGURE 20. (*a*) Trajectory, (*b*) projection of the velocity vector onto the horizontal plane and (*c*) the modulus of the Fourier transform (spectrum) of u_y for a dense sphere ($\rho_0/\rho = 5$) at $G = 250$.

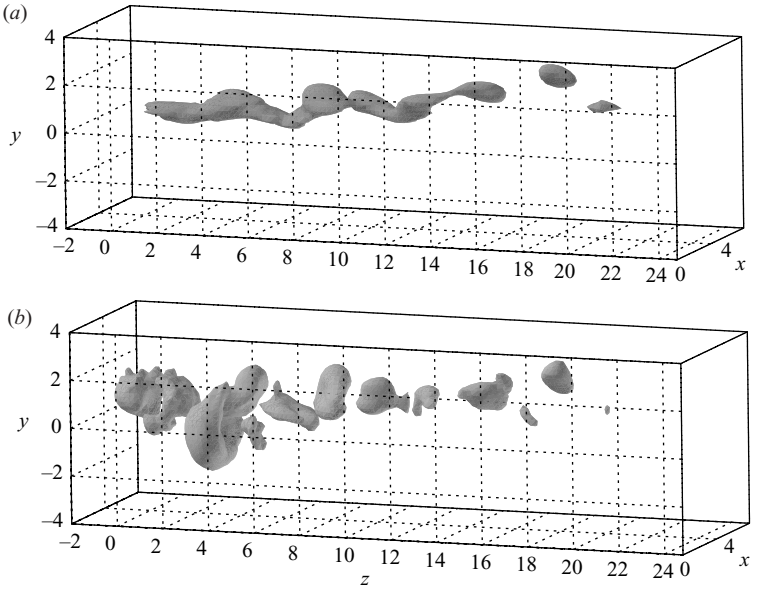

FIGURE 21. Non-axisymmetric perturbation (sum of azimuthal modes $m = 1$–6) in the chaotic regime at $G = 350$ and for $\rho_0/\rho = 3$. (*a*) Iso-surface of axial velocity $v_z = -0.16$. (*b*) Iso-surface of the pressure $p = -0.006$.

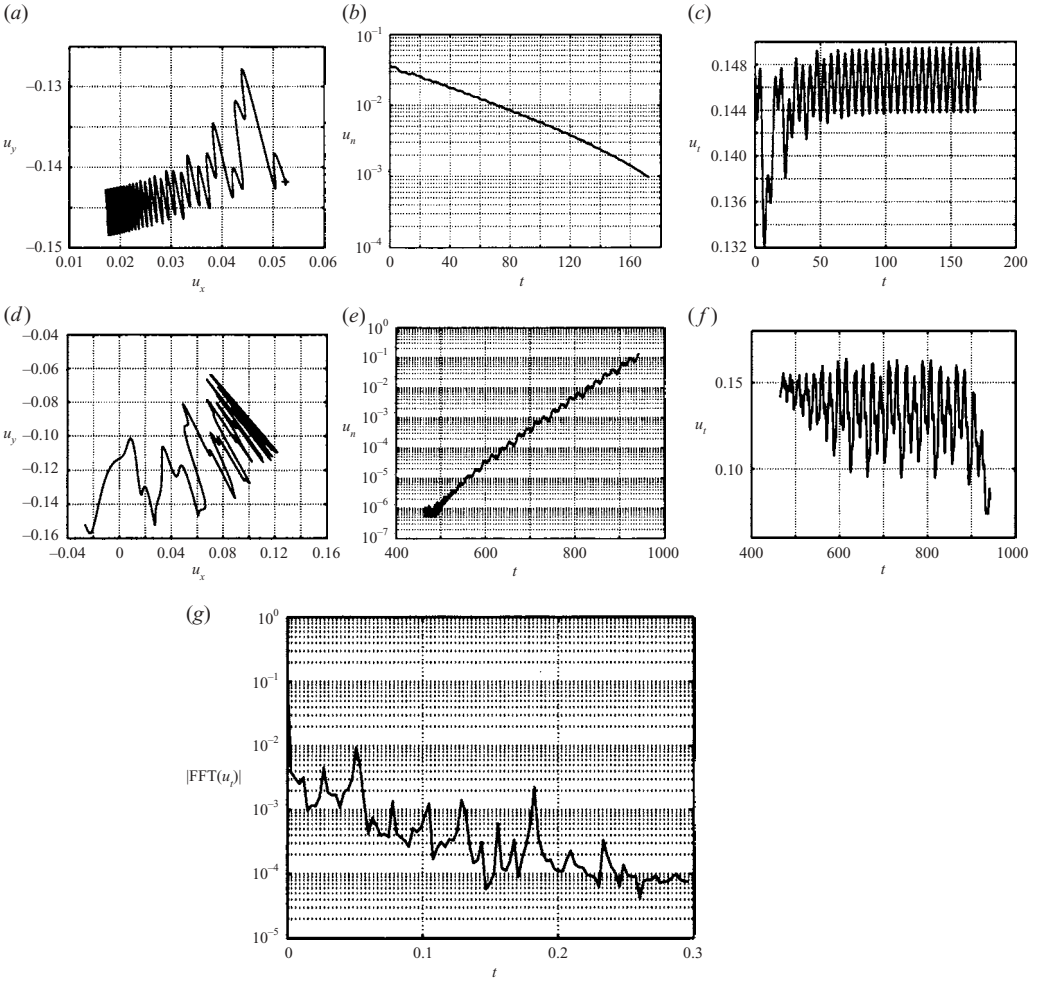

FIGURE 22. Onset of chaos for a dense sphere $\rho_0/\rho = 5$. (a, d) Horizontal projection of the sphere velocity vector, (b, e) Semi-logarithmic plot of the velocity component normal to the broken symmetry plane, (c, f) Horizontal component of the projection of the sphere velocity onto the broken symmetry plane. $(a–c)$ Relaxation of a perturbation to a subcritical state $(G = 210)$. $(d–f)$ Amplification of the three-dimensional perturbation above the threshold of the chaos $(G = 225)$. (g) Fourier transform of the velocity of figure (f).

These features are strikingly similar to that observed for Reynolds numbers exceeding 500 in the work of Tomboulides & Orszag (2000) for the flow past a fixed sphere. In that case, at $Re = 500$, a lower frequency ($St \approx 0.045$) was observed together with a higher one at $St = 0.167$. To simplify the comparison, let us remark that at $G = 225$ the mean vertical velocity of the falling sphere is about 1.41, i.e. its Reynolds number based on this velocity is $Re = 320$ and the Strouhal numbers of the frequencies f' and f are 0.035 and 0.13, respectively. The fact that, unlike in Tomboulides & Orszag (2000), the lower frequency dominates in figure 22(g) is not essential. The velocity field represented at a given point of the flow or a horizontal velocity component are just two selected degrees of freedom of a more complex system. The spatial envelopes of the modes oscillating with frequencies f and f' are certainly different and there are, very probably, points of the wake of the fixed sphere

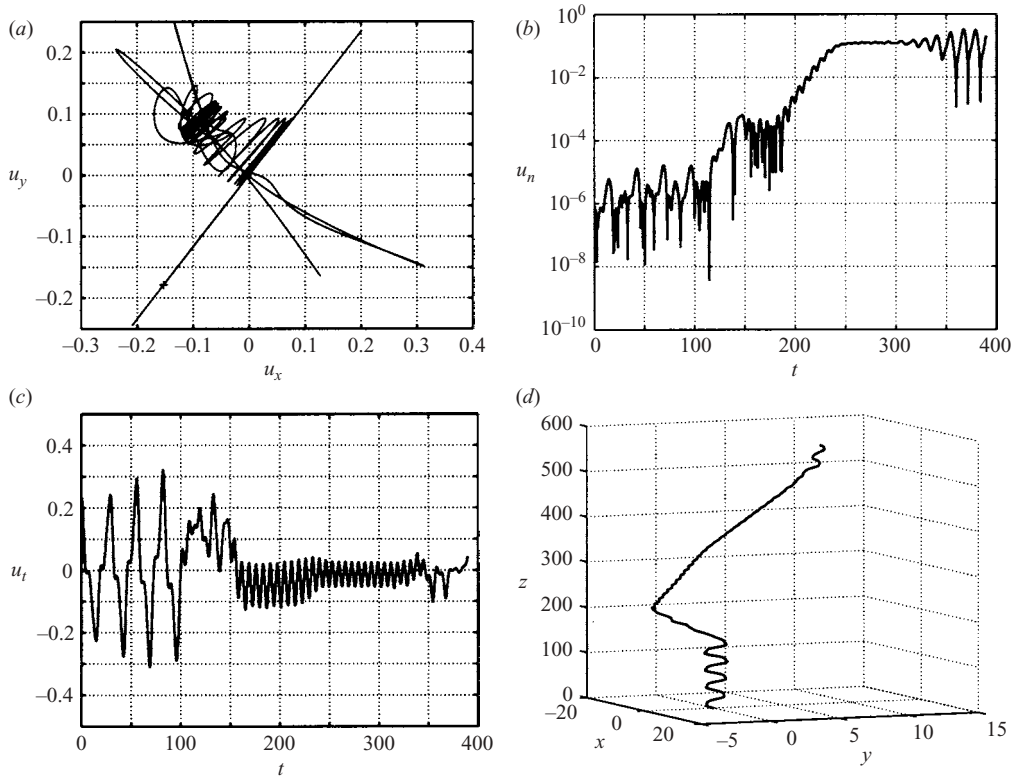

FIGURE 23. Onset of chaos for a light sphere $\rho_0/\rho = 0.5$ at $G = 225$. The threshold lies at $G \approx 215$. (*a*) The projection of the velocity vector onto the horizontal plane. (*b*) The projection of the velocity onto the normal direction to the broken symmetry plane. (*c*) The projection onto the symmetry plane. (*d*) The corresponding trajectory.

where the low frequency dominates (see also Dauchy, Dušek & Fraunié 1997). The density ratio of 5 was found in many respects to be practically equivalent to infinity (corresponding to a fixed sphere), moreover the same scenario applies to spheres of densities higher than 2.5 practically independently of the exact density ratio value. This might suggest extrapolating the results obtained concerning the transition to chaos to a fixed sphere wake. Nevertheless, a more detailed investigation of this limit would be of interest.

As for the light spheres, all that has already been illustrated in the case of the density ratio 5 still holds: the bifurcation is regular and leads to chaos and three-dimensionality of trajectories (see figure 23*a–d*). In figures 23(*a*) and 23(*d*), notice that before the trajectory leaves the symmetry plane the slow zigzagging state is destroyed. The long stage of rapid oscillations in figure 23(*c*) is practically periodic with frequency $f = 0.14$ typical for unstable oscillating perturbations of axisymmetric wake. The initial part of this stage corresponds to the exponential increase of the drifting velocity normal to the original symmetry plane in figure 23(*b*). (The rapid oscillations are visible even before the perpendicular velocity component emerges from the numerical noise. Even 'exactly' plane trajectories are plane only within an error of about 10^{-5}.) The drift of the velocity reaches saturation before the onset of a new, only intermittent, quasi-plane stage represented by the strong oscillations perpendicular to the initial direction in figure 23(*a*). In other words, the trajectory

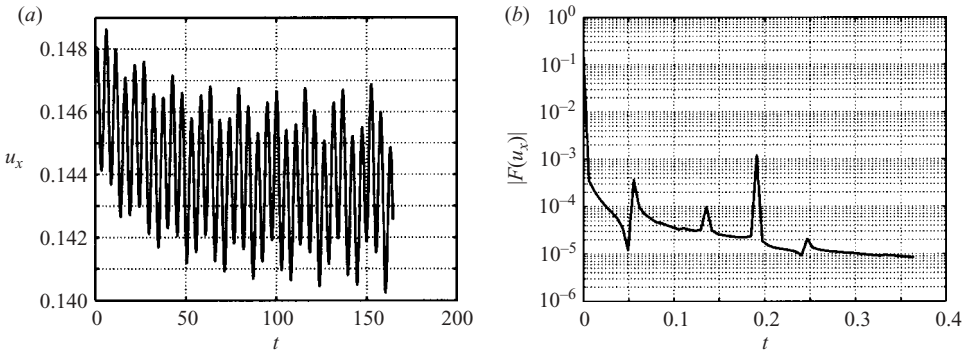

FIGURE 24. Simulation of a forced two-dimensional trajectory in the plane (Oxz) at $G = 225$ and $\rho_0/\rho = 10$. (a) Evolution of the horizontal sphere velocity u_x. (b) Fourier transform (spectrum) of the asymptotic regime. The visible frequencies are $f_2 = 0.0555$, $f_1 - f_2 = 0.1357$, $f_1 = 0.1912$ and $f_1 + f_2 = 0.2467$.

starts to zigzag (always roughly parallel to the initial plane, but no longer with a vertical mean velocity) with a smaller amplitude and with a higher frequency while drifting perpendicularly to the plane. Once the drifting velocity reaches saturation, the plane of the zigzagging motion switches direction and an intermittent spot characterized by low-frequency oscillations characteristic of the subcritical state sets in.

As a rule, a symmetry breaking bifurcation is inhibited if the symmetry it breaks is forced, i.e. the subcritical state remains stable in the subspace of symmetric states. This is not the case if the plane symmetry of the trajectory is forced above the threshold of the transition to chaos. The velocity of the sphere oscillates in the symmetry plane much like in figure 22(f) (see figure 24a). The spectra in figures 22(g) and 24(b) are very similar, with the three highest peaks at about same frequencies. (The densities correspond to dense spheres in both cases.) The spectrum in figure 24(b) is typical for a limit torus dynamics (see e.g. Dauchy *et al.* 1997) with two fundamental frequencies $f_1 \approx 0.19$ and $f_2 \approx 0.055$. (To prove rigorously that the frequencies are really incommensurate, it would be necessary to show that the frequency ratio evolves continuously as a function of G (see Dauchy *et al.* 1997) but this point is not essential for the present analysis.) The resemblance between the spectra in figure 22(g) and in figure 24(b) indicates that a Hopf bifurcation accompanies the regular one. The former exists in the subspace with enforced plane symmetry, the other in its linear complement. In the linear regime, these bifurcations are independent. The onset of chaos might be explained by the interaction of both bifurcations via the nonlinear coupling (see figure 23b, c).

In conclusion, the bifurcation (or, better, one of the bifurcations) at the origin of the chaos is of regular type. Among all classical scenarii of transition to chaos described in the literature (see e.g. Bergé, Pomeau & Vidal 1992) only the type I intermittency starts from a regular bifurcation. The asymptotic state presents, indeed, a typical intermittent behaviour (see § 8.3 and figures 23), but also figure 20(b) presents intermittent oscillations of the velocity interrupted by almost monotonous velocity variations. The typical case of type I intermittency requires a subcritical saddle-node bifurcation to trigger chaos. In this case, the regular bifurcation seems to be of a supercritical nature, the chaos resulting from an interplay with a coexisting Hopf bifurcation.

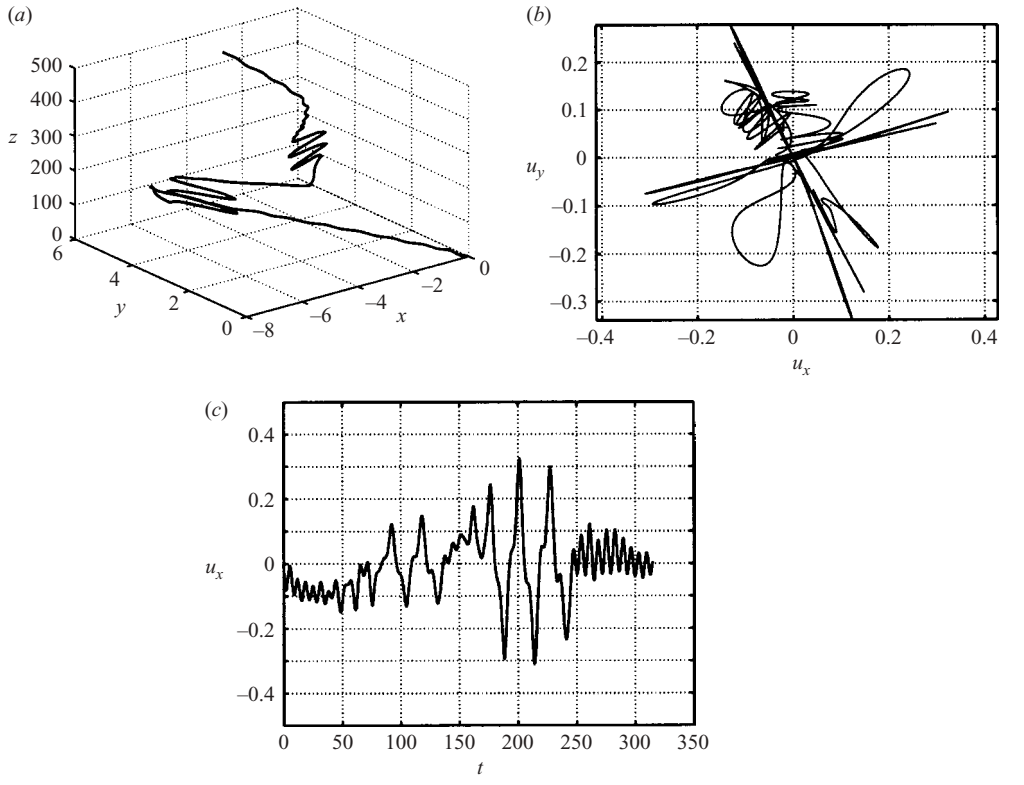

FIGURE 25. Intermittent three-dimensional state at $G = 220$ and $\rho_0/\rho = 0.5$. (*a*) Three-dimensional trajectory with two zigzagging spots. (*b*) Projection of the velocity vector onto the horizontal plane. The zigzagging spots correspond to the two quasi-plane stages. (*c*) u_x component of the sphere velocity *vs.* time.

8.3. *Investigation of the chaotic domain*

A typical trajectory presenting typical intermittent behaviour with two intermittent spots is presented in figure 25(*a*) for a light sphere $\rho_0/\rho = 0.5$ at $G = 220$, i.e. only slightly above the threshold of the transition to chaos. During these spots the trajectory resumes the subcritical zigzagging behaviour temporarily. The intermittent spots are characterized by large velocity fluctuations. It is thus easy to identify them in figure 25(*b*). The trajectory is quasi-plane during these stages. The pattern of the velocity *vs.* time curve of the zigzagging motion of figure 14(*b*) clearly reappears during the intermittent stages in figure 25(*c*). As already noted in the previous subsection, the characteristic frequency of the (aperiodic) oscillation in the chaotic and three-dimensional regime is quite different from that of the zigzagging motion. The rapid oscillations in figure 25(*c*) have again the frequency $f \approx 0.14$ (corresponding to the imaginary part of the unstable complex eigenvalue of the discretized linear operator based on the axisymmetric wake). For comparison, the slow zigzagging frequency is $f = 0.038$ and its third harmonic is $3f = 0.114$ (see § 7).

While investigating the parameter space in the chaotic domain we found one more striking feature of the dynamics of light spheres. To obtain the results of the parametric study more rapidly we ran several cases in parallel on a meta-computing cluster using the same subcritical (periodic) asymptotic state as initial conditions. For spheres

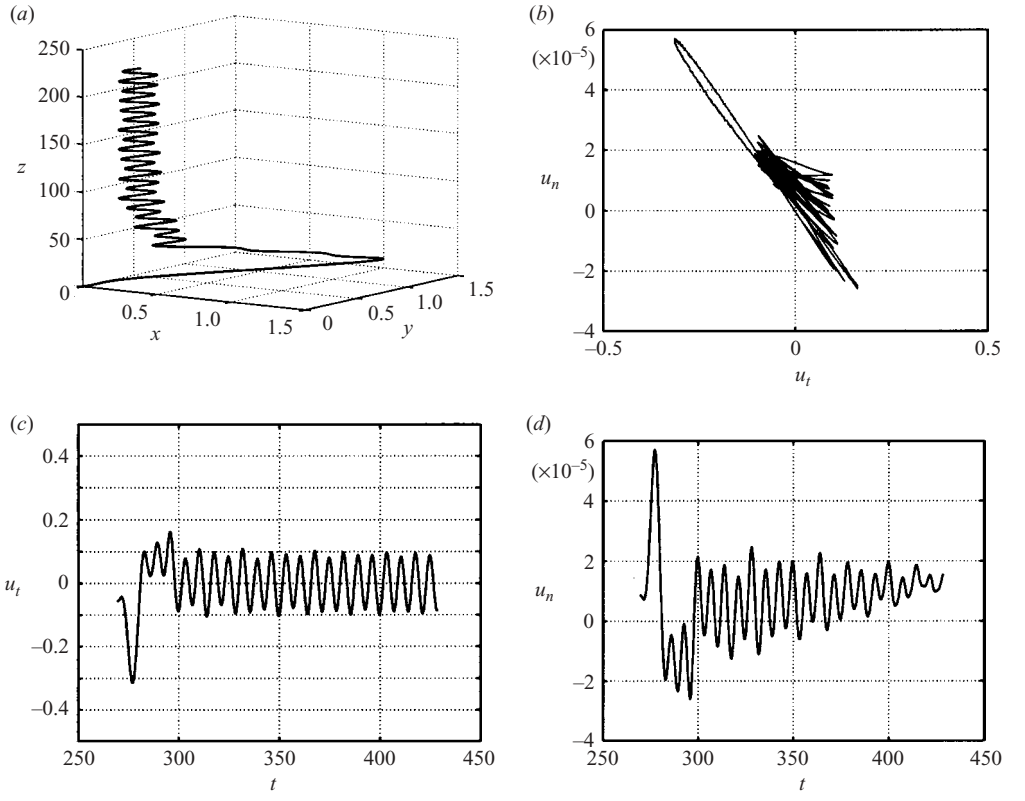

FIGURE 26. (*a*) Quasi-bidimensional trajectory at $G = 240$ and for $\rho_0/\rho = 0.5$ (critical value of G for the onset of chaos: $G_{crit} \approx 215$). (*b*) Horizontal projection of the velocity. (*c*, *d*) Tangential and orthogonal components of the velocity to the plane defined by the horizontal velocity at $t = 360$.

of density ratio 0 and 0.5 and in the intervals $215 < G < 275$ and $230 < G < 325$, respectively, the behaviour of the sphere was periodic and plane, the frequency corresponding to $f \approx 0.14$ (see the frequencies presented in the previous subsection). In figure 26 an example of such a simulation is given for $\rho_0/\rho = 0.5$ and $G = 240$. Figure 26(*b*) shows the projection of the velocity vector onto the normal direction to the plane of the trajectory. (Note the scale of the vertical axis.) figure 26(*d*) shows the diminishing trend of the oscillations in the normal direction indicating the stability of the planar trajectory. In figure 26(*c*), the trend to perfect periodicity is visible. To see if this result means that the chaotic states do not exist in this subdomain of the parameter space, we ran new simulations for the same parameter values, but starting from a fully developed chaotic state. The counterpart of figure 26 is presented in figure 27. The state presents no trend toward two-dimensionality and has the same intermittent features as that in figure 25. Clearly, in this subdomain of the parameter space, two stable states coexist.

This result might be important for experiments with very homogeneous spheres. As shown in figure 28, a sphere released from rest will not be perturbed enough to reach the chaotic state and will rather be attracted by the periodic one. For imperfectly homogeneous spheres this is much less likely to occur (see § 10).

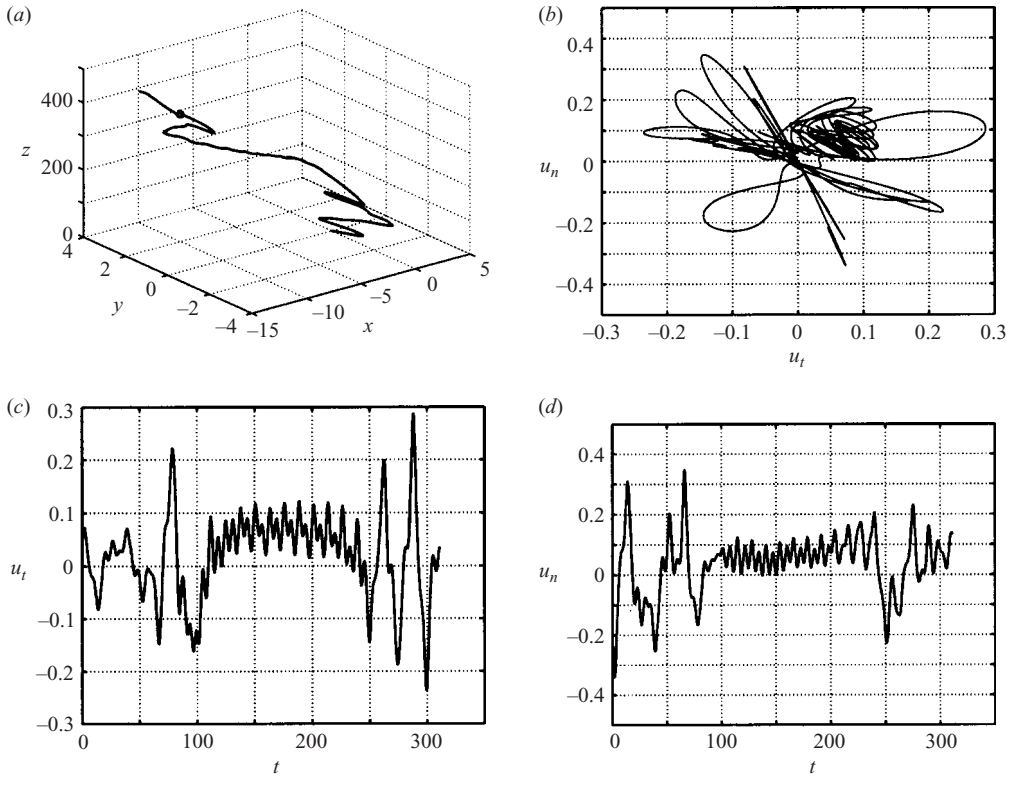

FIGURE 27. (*a*) Trajectory starting from a fully three-dimensional motion at $G = 240$ and for $\rho_0/\rho = 0.5$ (critical value of G for the onset of chaos: $G_{crit} \approx 215$). (*b*) Horizontal projection of the velocity. (*c*, *d*) Tangential and orthogonal components of the velocity to the plane defined by the horizontal velocity at $t = 360$.

9. Diagram in the parameter space

In the previous sections, we showed that all spheres reach, progressively, with increasing Galileo numbers, a steady oblique and an oblique periodic regime before starting to move chaotically. We made it qualitatively clear that the thresholds of the various regimes depend on the density ratio ρ_0/ρ. Moreover, only 'light' spheres present a zigzagging state. We stated that the oblique periodic regime is characterized by two different frequencies, a lower one for light spheres and a higher one for spheres of higher density. It is necessary to make a chart of the different regimes in the $G - \rho_0/\rho$ parametric space. This chart is provided in figure 29 summing up the simulation of 81 different asymptotic regimes.

In agreement with expectations, the factor ρ_0/ρ in the equations of motion (2.4*a*) and (2.4*b*) plays a more important role as the regimes change from steady to unsteady and the acceleration of the sphere is more significant. The domain of the periodic oblique regime is separated into two parts by a roughly horizontal line at $\rho_0/\rho = 2.5$. For spheres with a density ratio lower than 2.5, the frequency of oscillations is $f \approx 0.065$ (i.e. the Strouhal number is $St \approx 0.048$), while for spheres with a higher density ratio this frequency is $f \approx 0.175$ ($St \approx 0.130$). The limit of existence of the zigzagging periodic regime seems to lie exactly at the density ratio of one, i.e. the zigzagging regime exists only for ascending spheres. The delimitation of the subdomain

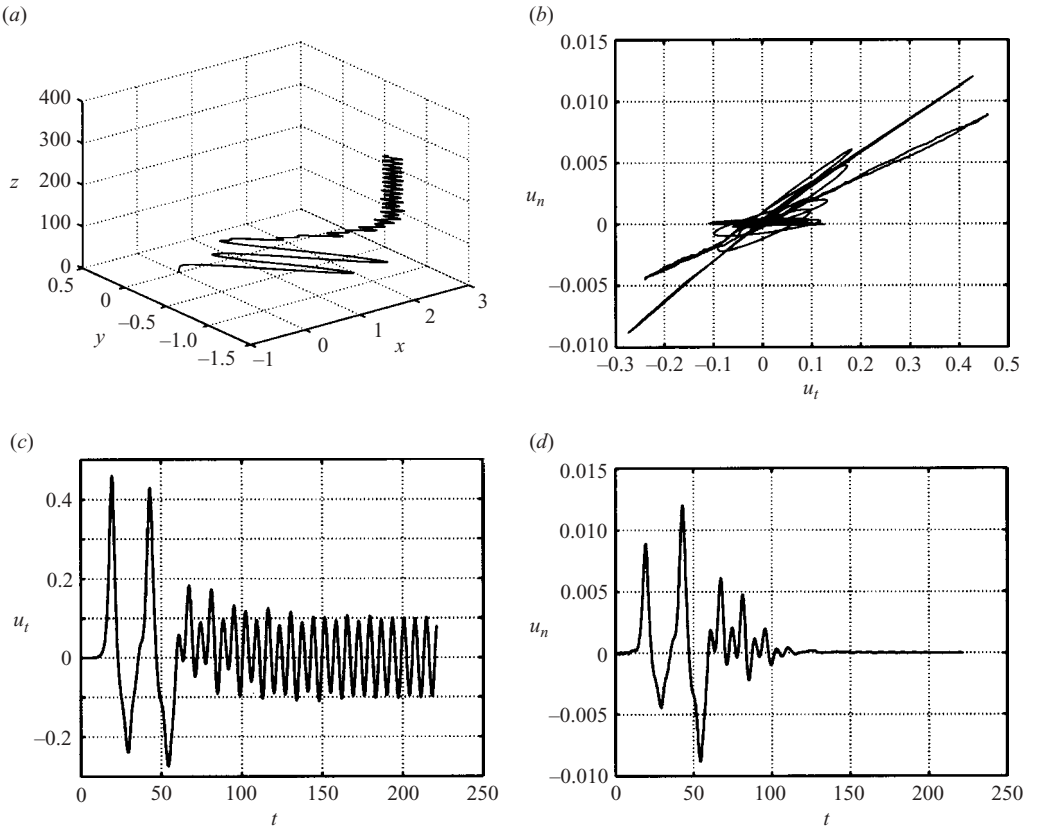

FIGURE 28. (*a*) Full trajectory starting at rest at $G = 250$ and for $\rho_0/\rho = 0.5$ (Critical value of G for the onset of chaos: $G_{crit} \approx 215$). (*b*) Horizontal projection of the velocity. (*c*, *d*) Tangential and orthogonal components of the velocity to the plane defined by the horizontal velocity at $t = 200$.

in which two asymptotic regimes coexist is only tentative. We did not make detailed simulations close to the density ratio 1 to prove that this value is the exact limit. Nevertheless, no similar case was found for any density ratio greater than or equal to 1.3. At the Galileo number of 350 (i.e. at particulate Reynolds numbers of about 500) the periodic states coexisting with chaos were no longer in evidence.

10. Not perfectly homogeneous spheres

In § 3, we described preliminary experiments with polypropylene balls used in bearings. Measurements proved the very good sphericity of the balls and also the masses of the spheres appeared to be quite reliable in view of a good agreement of the measured and computed ascension velocities. For the dynamics of unsteady regimes it is, nevertheless, crucial that the moment of inertia in (2.4) be correctly established. Our simulations were up to now based on the assumption that the spheres are perfectly homogeneous. However, when we broke some of the bearing balls we found a small air bubble trapped eccentrically in the plastic. As a result, the geometrical centre and the centre of mass of the balls do not coincide. To assess the impact of such an imperfection we implemented a variable eccentricity of the centre of mass into the code. This is easily done by adding the term $\boldsymbol{x}_{\mathrm{exc}} \times \boldsymbol{F}_{fl}$ to the torque on the right-hand

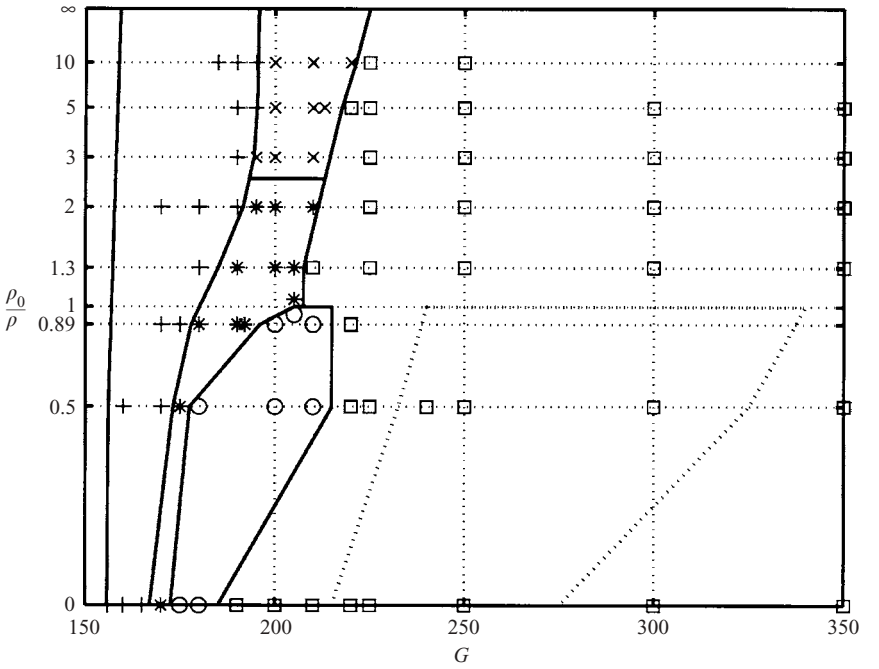

FIGURE 29. Diagram of the asymptotic states of the trajectory of a free sphere. The vertical axis is plotted proportionally to $(\rho_0-\rho)/(\rho_0+\rho)$, but is labelled in ρ_0/ρ. To the left of the primary bifurcation (leftmost line) the wake is axisymmetric. The symbols denote the simulations: +, steady and oblique; *, oblique and oscillating regime with low frequency ($0.045 \leqslant f \leqslant 0.068$); ×, oblique and oscillating regime with high frequency ($f \approx 0.180$); ○, zigzagging periodic regime ($0.023 \leqslant f \leqslant 0.035$); □, three-dimensional chaotic regime. The domain of coexistence of a chaotic and a periodic state ($f = 0.14$) is approximately delimited by the dotted line.

side of (2.4). $\boldsymbol{x}_{\mathrm{exc}}$ stands for the vector linking the centre of mass of the sphere to its geometrical centre, at which the hydrodynamic force $\boldsymbol{F}_{fl}$ acts assuming the sphere has a perfectly spherical shape.

Figures 30 and 31 show that, naturally, if the initial position of the centre of mass does not correspond to a static equilibrium (we place it horizontally with respect to the geometrical centre) the swinging movement of the sphere brings about oscillations visible in the initial stages of the trajectory. Moreover, this pendulum movement has a destabilizing effect on the system. Figures 30 and 31 compare the perfect and imperfect sphere for the density ratio 0.5 for two values of the Galileo number $G = 170$ and $G = 200$, respectively. In figure 30, the trajectory of the non-homogeneous sphere, instead of being steady and oblique, becomes oblique and oscillating, i.e. it is already undergoing the secondary bifurcation. In figure 31, instead of a zigzagging regime a chaotic state is obtained. The trend for the non-homogeneous spheres is thus to undergo the bifurcations more rapidly. This explains why the experimental trajectories in § 3 are chaotic although the Galileo number is only $G = 180$.

11. Conclusions

Our numerical simulations show that the system represented by a freely falling or freely ascending sphere under the action of gravity in a Newtonian fluid undergoes a transition to a full spatio-temporal chaos in the range of Galileo numbers lying

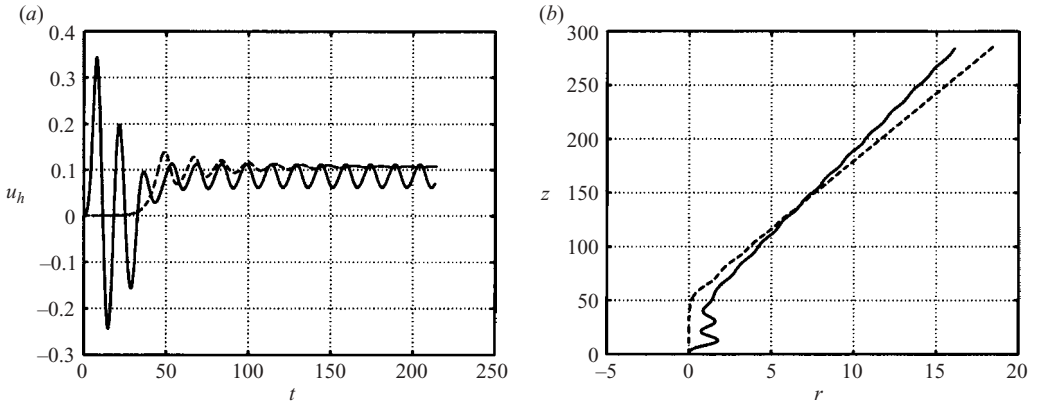

FIGURE 30. Trajectory of a homogeneous sphere and a sphere having its centre of mass at 0.025 diameters from the geometric centre at $G = 170$ and for $\rho_0/\rho = 0.5$. (*a*) Horizontal component of the velocity of a homogeneous (dashed line) and inhomogeneous sphere (solid line). (*b*) Planar trajectories of a homogeneous (dashed line) and inhomogeneous sphere (solid line).

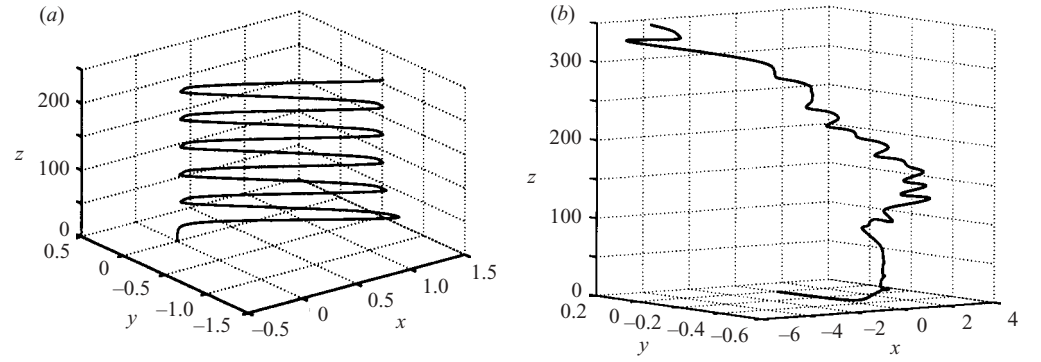

FIGURE 31. Trajectory of an ascending sphere at $G = 200$ and $\rho_0/\rho = 0.5$. (*a*) Homogeneous sphere. (*b*) Inhomogeneous sphere : the centre of mass is at 0.025 diameters from the geometric centre of the sphere.

between $G = 150$ and $G = 225$, i.e. in terms of asymptotic average Reynolds number, between 205 and 310. The scenario is significantly different for falling and for ascending spheres.

For very dense falling spheres, the results obtained are in perfect agreement with the results of simulation of the fixed sphere wake, the latter corresponding to spheres of infinite density. The primary (regular, axisymmetry breaking) and the secondary (Hopf) bifurcations are found at the same thresholds. Moreover, the loss of periodicity is found to coincide with that of planarity of the trajectories and, in agreement with Mittal (1999*b*), with the loss of planar symmetry of the wake. At the opposite limit of the density scale, the results found are in agreement with the bibliographical data concerning spherical bubbles of Wu & Gharib (2002) reporting a zigzagging regime and with those concerning light spheres of Lunde & Perkins (1997) reporting an intermittent behaviour. Further validations are obtained using our own experimental data (figure 1). Excellent agreement is reached in the steady oblique regime (Jenny & Dušek 2004), but discrepancies appear when the behaviour for a given Galileo number

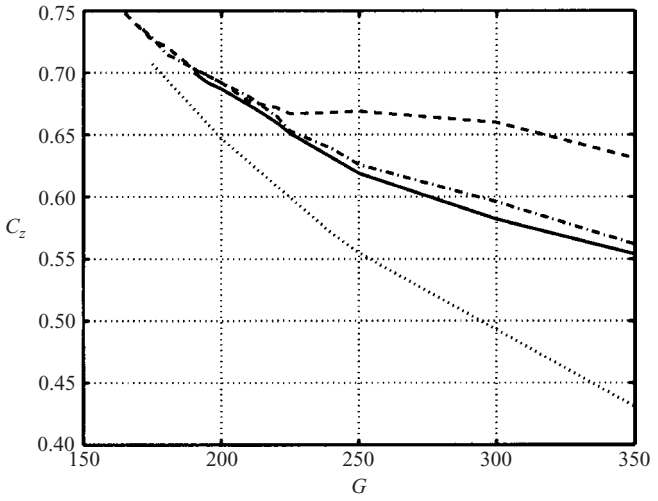

FIGURE 32. Mean drag coefficient $C_z = 4/(3U_z^2)$ *vs.* G for reduced densities, $\rho_0/\rho = 0$ (dashed line), $\rho_0/\rho = 0.5$ (dash–dotted line) and $\rho_0/\rho = 5$ (solid line). The dotted line plots the drag coefficient of the axisymmetric wake.

and a given density ratio is compared between experimental observations of § 3 and the numerical results in unsteady regimes. Section 10 provides an explanation in terms of imperfections of mass distribution of experimental spheres. At the same time, the considerable impact of slight imperfections on the transition scenario underlines the necessity of a further experimental investigation allowing other effects potentially responsible for differences in behaviour of ideally perfect and of real experimental spheres to be detected.

Whatever the results of this experimental investigation, it is practically impossible to confirm the results of Karamanev (2001). Although, the instabilities definitely enhance the (average) drag coefficient, the increase is far from what is found by Karamanev *et al.*

The real impact of the transition on many particle systems will certainly consist of a considerable modification of their dispersion characteristics. The spheres have a trend to drift horizontally by themselves without interacting, and in the chaotic regime, they are very receptive to perturbations. To simulate such systems, appropriate numerical algorithms are available. Hu *et al.* (2001) and Glowinski *et al.* (2001) provided an adaptation to account for very light particles. However, in view of the complexity of the transition dynamics, the question of whether the numerical costs are not still too high may be crucial for such a project.

The authors are grateful for being able to run some of the numerical simulations on the MetaCenter supercomputing facilities provided under the research grant MSM 000000001 of the Czech Republic.

REFERENCES

BERGÉ, P., POMEAU, Y. & VIDAL, C. 1992 *L'Ordre dans le Chaos.* Collection Enseignement des Sciences, Hermann.

BOZZI, L. A., FENG, J. Q., SCOTT, T. C. & PEARLSTEIN, A. J. 1997 Steady axisymmetric motion of deformable drops falling or rising through a homoviscous fluid in a tube at intermediate Reynolds number. *J. Fluid Mech.* **336**, 1–32.

Dauchy, C., Dušek, J. & Fraunié, P. 1997 Primary and secondary instabilities in the wake of a cylinder with free ends. *J. Fluid Mech.* **332**, 295–339.

Duineveld, P. 1995 The rise velocity and shape of bubbles in pure water at high Reynolds number. *J. Fluid Mech.* **292**, 325–332.

Dušek, J., Fraunié, P. & Le Gal, P. 1994 A numerical and theoretical study of the first Hopf bifurcation in a cylinder wake. *J. Fluid Mech.* **264**, 59–80.

Ellingsen, K. & Risso, F. 2001 On the rise of an ellipsoidal bubble in water: oscillatory paths and liquid-induced velocity. *J. Fluid Mech.* **440**, 235–268.

Fortes, A., Joseph, D. & Lundgren, T. 1987 Nonlinear mechanics of fluidization of beds of spherical particles. *J. Fluid Mech.* **177**, 467–483.

Ghidersa, B. & Dušek, J. 2000 Breaking of axisymmetry and onset of unsteadiness in the wake of a sphere. *J. Fluid Mech.* **423**, 33–69.

Glowinski, R., Pan, T., Hesla, T., Joseph, D. & Périaux, J. 2001 A fictitious domain approach to the direct numerical simulation of incompressible viscous flow past moving rigid bodies : application to particulate flow. *J. Comput. Phys.* **169**, 363–426.

Goldburg, A. & Florsheim, B. 1966 Transition and Strouhal number for the incompressible wake of various bodies. *Phys. Fluids* **9**, 45–50.

Hu, H. H., Patankar, N. A. & Zhu, M. Y. 2001 Direct numerical simulations of fluid–solid systems using the arbitrary Lagrangian–Eulerian technique. *J. Comput. Phys.* **169**, 427–462.

Jenny, M., Bouchet, G. & Dušek, J. 2003 Non vertical ascension or fall of a free sphere in a newtonian fluid. *Phys. Fluids* **15**, L9–L12.

Jenny, M. & Dušek, J. 2004 Efficient numerical method for the direct numerical simulation of the flow past a single light moving spherical body in transitional regimes. *J. Comput. Phys.* **194**, 215–232.

Johnson, T. & Patel, V. 1999 Flow past a sphere up to a Reynolds number of 300. *J. Fluid Mech.* **378**, 19–70.

Karamanev, D. 1996 Equations for calculation of the terminal velocity and drag coefficient of solid spheres and gas bubbles. *Chem. Engng Commun.* **147**, 75–84.

Karamanev, D. 2001 The study of free rise of buoyant spheres in gas reveals the universal behaviour of free rising rigid spheres in fluid in general. *Intl J. Multiphase Flow* **27**, 1479–1486.

Karamanev, D., Chavarie, C. & Mayer, R. 1996 Dynamics of the free rise of a light solid sphere in liquid. *AIChE J.* **42**, 1789–1792.

Karamanev, D. & Nikolov, L. 1992 Free rising spheres do not obey Newton's law for free settling. *AIChE J.* **38**, 1843–1846.

Lunde, K. & Perkins, R. J. 1997 Observations on wakes behind spheroidal bubbles and particules. *ASME Fluids Engng Division Summer Meeting*, FEDSM'97 (FEDSM97-3530).

Magarvey, R. & Bishop, R. 1961 Wakes in liquid–liquid systems. *Phys. Fluids* **4**, 800–804.

Magarvey, R. & MacLatchy, C. 1965 Vortices in sphere wakes. *Can. J. Phys.* **43**, 1649–1656.

Magnaudet, J. 1997 The forces acting on bubbles and rigid particles. *ASME Fluids Engng Division Summer Meeting*, FEDSM'97, pp. 1–9.

Mittal, R. 1999*a* A Fourier–Chebyshev spectral collocation method for simulating flow past spheres and spheroids. *Intl J. Numer. Meth. Fluids* **30**, 921–937.

Mittal, R. 1999*b* Planar symmetry in the unsteady wake of a sphere. *AIAA J.* **37**, 388–390.

Mordant, N. & Pinton, J.-F. 2000 Velocity measurement of a settling sphere. *Eur. Phys. J.* B **18**, 343–352.

Mougin, G. & Magnaudet, J. 2002*a* The generalized Kirchhoff equations and their application to the interaction between a rigid body and an arbitrary time-dependent viscous flow. *Intl J. Multiphase Flow* **15**, 1837–1851.

Mougin, G. & Magnaudet, J. 2002*b* Path instability of a rising bubble. *Phys. Rev. Lett.* **88**, 014502.

Natarajan, R. & Acrivos, A. 1993 The instability of the steady flow past spheres and disks. *J. Fluid Mech.* **254**, 323–344.

Ormières, D. 1999 Etude expérimentale et modélisation du sillage d'une sphère à bas nombre de Reynolds. PhD thesis, Université de Provence.

Ormières, D. & Provansal, M. 1999 Transition to turbulence in the wake of a sphere. *Phys. Rev. Lett.* **83**, 80–83.

Sreenivasan, K. R., Strykowski, P. J. & Olinger, D. J. 1987 Hopf bifurcation, Landau equation and vortex shedding behind circular cilynders. *ASME Applied Mech. Bio Engng and Fluid Engng Conf. Cincinnati, Ohio, June 11–17*, vol 52. (ASME FED).

Thompson, M., Leweke, T. & Provansal, M. 2001 Kinematics and dynamics of sphere wake transition. *J. Fluids Structures* **15**, 575–585.

Tomboulides, A. G. & Orszag, S. A. 2000 Numerical investigation of transitional and weak turbulent flow past a sphere. *J. Fluid Mech.* **416**, 45–73.

Williamson, C. H. K. 1989 Oblique and parallel modes of vortex shedding in the wake of a circular cylinder at low Reynolds numbers. *J. Fluid Mech.* **206**, 579–627.

Wu, M. & Gharib, M. 2002 Experimental studies on the shape and path of small air bubbles rising in clean water. *Phys. Fluids* **14**, L49–L52.